

**UNIVERSITY OF SOUTHAMPTON**

# **Applications of Microfluidics in Nuclear Magnetic Resonance**

by

William G Hale

A thesis submitted in partial fulfillment for the  
degree of Doctor of Philosophy

in the  
Faculty of Engineering and Physical Sciences  
School of Chemistry

June 2019



UNIVERSITY OF SOUTHAMPTON

ABSTRACT

FACULTY OF ENGINEERING AND PHYSICAL SCIENCES  
SCHOOL OF CHEMISTRY

Doctor of Philosophy

by William G Hale

Microfluidics is a constantly growing field of research, finding applications in a diverse range of subjects such as materials science, chemistry and across the life sciences. This expansion is due to many advantageous attributes: small sample volumes which contribute to waste reduction and reduced cost of experimentation; highly controllable local environments that enable very precise investigation of changes in systems to stimuli; rapid prototyping techniques that mean make, test, tweak cycles can be run more than once in a typical day; ease of parallelisation makes gathering statistically significant data much easier without the need to repeat experiments for days at a time; and ease of automation increases precision and repeatability.

Nuclear magnetic resonance (NMR) spectroscopy is a widely applied technique in chemistry and the life sciences. Its non-invasive and non-destructive nature makes NMR ideal to study living, or mass limited samples. NMR, however, requires an extremely homogeneous magnetic field to enable molecular structure determination and can be limited by the inherent low sensitivities possible in a typical experiment.

This thesis describes methods for integrating these two fields. Some NMR experiments being ‘miniaturised’ to be performed ‘on-chip’ as well as microfluidic concepts that have been engineered to be compatible with NMR techniques. These techniques do not seek to replace established methods of microfluidic analysis such as mass spectrometry or fluorescence spectroscopy but could be used to compliment these techniques as an additional method of extracting data from a system.



# Contents

<b>Nomenclature</b>	vii
<b>Acknowledgements</b>	ix
<b>1 Parahydrogen induced polarization on a chip</b>	1
1.1 Synopsis . . . . .	1
1.2 Introduction . . . . .	2
1.3 Hyperpolarization . . . . .	4
1.3.1 Sensitivity . . . . .	4
1.3.2 Hyperpolarization . . . . .	4
1.3.3 Techniques . . . . .	5
1.3.3.1 Brute Force . . . . .	5
1.3.3.2 Dynamic Nuclear polarization . . . . .	5
1.4 Parahydrogen Induced polarization - PHIP . . . . .	6
1.4.1 Parahydrogen . . . . .	6
1.4.2 PASADENA and ALTADENA . . . . .	9
1.4.2.1 Spin Physics . . . . .	10
1.5 Materials and methods . . . . .	14
1.6 Results and Discussion . . . . .	16
1.6.1 Parahydrogen relaxation in PDMS . . . . .	16
1.6.2 Reaction Scheme . . . . .	17
1.6.3 ALTADENA . . . . .	17
1.6.4 PASADENA . . . . .	18
1.6.5 Signal Analysis . . . . .	21
1.6.6 Hydrogen Transport . . . . .	22
1.6.7 Sensitivity and Limit of Detection . . . . .	23
1.6.8 2D NMR . . . . .	27
1.7 Conclusions . . . . .	30



# Nomenclature

$a$	The signal amplitude
$\mathbb{B}$	The Boltzmann factor
$B_0$	The external magnetic field
$B_1$	The magnetic field produced by an NMR coil
$c_s$	The concentration of spins in a sample
$C$	A constant in SNR
$d$	The coil diameter
$F$	The noise factor from the spectrometer
<b>H</b>	The magnetic field
$h$	Planck's constant
$\hbar$	The reduced Planck constant
$\hat{H}$	The Hamiltonian operator in natural units
$I$	The spin quantum number
$\hat{I}$	The spin angular momentum operator
$i_c$	The current
$J$	The rotational quantum number
$k_0$	A constant that accounts for spatial inhomogeneities in the $B_1$ field
$k_B$	The Boltzmann constant
$l$	The length of a coil
$M_0$	The net magnetisation
$M_a$	The magnetisation vector component along the $a$ -axis
<b>M</b>	The magnetisation
$n_s$	The number of spins in a sample
$\check{\mathbf{n}}$	The surface normal
$p$	The polarisation of a spin system
$P_\alpha$	The population of the $\alpha$ state
$R_{\text{noise}}$	The dissipative loses
$\hat{R}$	The rotation operator
$S(t)$	The signal in the time domain
$S(\Omega)$	The signal in the frequency domain
$T$	The absolute temperature
$T_1$	The longitudinal relaxation time constant

$T_2$	The transverse relaxation time constant
$U$	The scalar magnetic potential
$V_s$	The sample volume
$V'_s$	The product of $k_0$ and $V_s$ that is the volume is within 10% of maximum
$\mathbb{1}$	The identity matrix
$\alpha_F$	The filling factor
$\beta_p$	The tilt of the roatation axis from $z$ for an off-resonance pulse
$\gamma_j$	The gyromagnetic ratio for a nucleus, $j$
$\delta$	The chemical shift
$\delta_{\text{RF}}$	The RF current penetration depth
$\Delta f$	The spectral bandwidth
$\epsilon$	The enhancement factor
$\theta$	The tilt angle of magentisation
$\theta_{\text{RF}}$	The angle between the r.f. coil and $B_0$
$\lambda_l$	The decay constant of a spin $l$
$\mu$	The reduced mass
$\mu_0$	The vacuum permeability
$\hat{\mu}$	magnetic dipole moment operator
$\xi$	The emf
$\rho_r$	The resistivity
$\hat{\rho}$	The density operator
$\sigma$	The chemical shielding factor
$\phi_p$	The phase of an r.f. pulse
$\phi_{\text{ref}}$	The phase shift in the rotating frame
$\Phi$	The angle that connects the static to rotating frame
$\chi_V$	The Magnetic susceptibility
$\omega_j^0$	The larmour frequency for a nucleus, $j$
$\omega_{\text{nut}}$	The nutation frequency
$\omega_{\text{ref}}$	The rotating frame frequency
$\Omega^0$	The and rotating frame frequency offset

## Acknowledgements

I would like to express my deep gratitude to Professor Marcel Utz for providing patient guidance and enthusiastic encouragement, as well as engaging discussion concerning all matters of life and work. His depth of knowledge in all manner of subjects was a great help throughout my PhD and provided a seemingly endless source of ideas and problem solving. The principles of scientific investigation I have learnt from him will stay with me throughout my career.

I wish to thank Professor Malcolm Levitt for his support and guidance, the discussions we have had about science helped me to see problems in a different light and increased my effectiveness as a scientist.

I am grateful to my colleagues who have helped me enormously throughout my time in Southampton in no particular order I wish to thank: James Eills, Graeme Finch, Rachel Greenhalgh, Benno Meir, Javier Alonso-Valdesueiro, Karel Kouril, Hana Kourilova, Aliki Moysiadi, Stuart Elliot, Christian Bengs, Manvendra Sharma, Bishnubatra Partra, Matheus Rossetto, Gabriel Rossetto, Marek Plata, Sylwia Ostrowska, Weidong Gong, Mohammed Sabba, George Bacanu, Laurynas Dagys, Jo Collel and Barbara Ripka.

To the people that provided support and encouragement throughout my work and helped me keep sane, I am indebted to Frankie Leeming, Thomas Kear, Laura Jowett, James Eills, Stuart Elliot, Christian Bengs, Aliki Moysiadi, Nic Charles, Judy Fox, Josie Charles, Gemma Charles and Eddie Robinson you all helped immensely.

In particular I'd like to thank Alyssa Charles for her unwavering support, encouragement, and belief in me, as well as proof reading and correcting my grammar errors.

Finally, I'd like to thank my family for all their support over the years, this is only possible because of them.



*To my friends and family*



# Chapter 1

## Parahydrogen induced polarization on a chip

This chapter is an extended version of J Eills\*, W Hale\*, M Sharma, M Rossetto, M H Levitt and M Utz, High-Resolution Nuclear Magnetic Resonance Spectroscopy With Picomole Sensitivity by Hyperpolarisation On A Chip, *Journal of the American Chemical Society*, 2019, XXXX, XXX, XXX-XXX [1]

### 1.1 Synopsis

In this chapter a device that combines high-resolution NMR and parahydrogen induced hyperpolarization (PHIP) with a high-sensitivity transmission line micro-detector is discussed. The para-enriched hydrogen gas is introduced into solution by diffusion through a membrane integrated into a microfluidic chip. NMR microdetectors, operating with sample volumes of a few  $\mu\text{l}$  or less, benefit from a favourable scaling of mass sensitivity discussed in ???. However, the small volumes make it very difficult to detect species present at less than millimolar concentrations in microfluidic NMR systems.

In view of overcoming this limitation, parahydrogen-induced polarization (PHIP) is implemented on a microfluidic device with 2.5  $\mu\text{l}$  detection volume. Integrating the hydrogenation reaction into the chip minimises polarization losses to spin-lattice relaxation, allowing the detection of picomoles of substance. This corresponds to a concentration limit of detection of better than  $1\mu\text{M}\sqrt{\text{s}}$ , unprecedented at this sample volume. The stability and sensitivity of the system can be used to extract quantitative information on the hydrogenation kinetics and their interplay with nuclear relaxation. It is further exemplified by homo- ( $^1\text{H}-^1\text{H}$ ) and heteronuclear ( $^1\text{H}-^{13}\text{C}$ ) 2D NMR experiments at natural  $^{13}\text{C}$  abundance.

## 1.2 Introduction

High-resolution NMR spectroscopy is a superbly versatile method which provides detailed and quantitative information on chemical composition and structure. It is widely used to follow the progress of chemical reactions [2, 3], as well as metabolic processes in living systems [4–7]. However, NMR suffers from inherently low sensitivity, which is due in part to the very weak polarization of nuclear spins along the magnetic field for samples in thermal equilibrium at ambient conditions. Conventional high-resolution NMR therefore requires nanomole quantities of sample. Many important problems require detection of analytes at low micromolar concentrations, such as transient reaction intermediates, or metabolic species. Despite the comparatively higher mass sensitivity of NMR for small sample volumes [8, 9], conventional micro-NMR systems around  $1 \mu\text{L}$  achieve mass limits of detection of no better than [10]  $1 \text{ nmol}\sqrt{\text{s}}$ , corresponding to a concentration limit of detection of  $1 \text{ mM}\sqrt{\text{s}}$ . An increase of several orders of magnitude in sensitivity is therefore required to enable NMR studies of mass-limited samples at micromolar concentrations.

Microfluidic lab-on-a-chip devices are finding increasing applications in chemistry and the life sciences. They provide detailed control over the experimental conditions at a much smaller length scale than conventional reactors, and allow integration of synthesis, separation, and analytical steps on a single platform [11–18]. The small size also affords the possibility of high experimental throughput. In the life sciences, microfluidic devices are increasingly used as sophisticated culture platforms for cells, cell assemblies, tissues, and small organisms [19–24]. The integration of NMR with microfluidics [10, 25–27] is promising, as it enables in-situ, non-invasive monitoring of chemical and metabolic processes in lab-on-a-chip systems.

The usefulness of microfluidic NMR could be significantly enhanced if the following conditions could be met: (i) sample volumes around  $1 \mu\text{l}$  or less; (ii) a concentration limit of detection near  $1 \mu\text{M}\sqrt{\text{s}}$ ; and (iii) spectral resolution of better than  $0.01 \text{ ppm}$  to allow distinction and identification of chemical species.

Although exquisitely sensitive NMR detection schemes exist, approaching even single-spin detection in favourable cases [28–38], they lack spectral resolution. While a recent study has demonstrated resolution of  $J$  couplings using a nitrogen-vacancy (NV) centre magnetometer. [39], none of these alternative detection schemes are compatible with high (several Tesla) magnetic fields, which are essential to produce spectral dispersion by chemical shifts. So far, no method has been demonstrated with the combination of high spectral resolution, high chemical dispersion, and high sensitivity for small volumes required for advanced microfluidic NMR measurements significantly below the  $1 \text{ mM}$  concentration scale.

Hyperpolarization methods generate substances which exhibit a transiently high level of nuclear spin polarization, with an increase in the NMR signal strength of more than 4 orders of magnitude [40], can be combined with micro-NMR detectors and microfluidic systems [41–48]. One such method involves the chemical reaction of the singlet spin isomer of molecular hydrogen, and is called parahydrogen-induced hyperpolarization (PHIP) [49–52].

While most studies have so far brought the reaction liquid in direct contact with hydrogen gas either through bubbling or by atomisation of the liquid in a hydrogen-filled chamber [53–59], liquid-gas interfaces and in particular bubbles pose difficulties in the context of microfluidic devices, since they tend to alter the flow properties, and can block fluid transport altogether. Continuous delivery of parahydrogen by diffusion through gas-permeable membranes has been demonstrated at conventional size scales [60, 61]. It has been shown that silicone elastomer membranes can be used to deliver parahydrogen directly to a flowing liquid in a microfluidic device [47]. Bordonali et al[48] have recently combined a microfluidic NMR probe system with a gas exchange chip based on a silicone elastomer membrane to implement the SABRE (signal enhancement by reversible exchange) variant of parahydrogen-induced polarization, but achieved only small signal enhancement factors (3 to 4).

In distinction from previous work [53–59, 61], this work integrates the hydrogenation reactor into the chip itself, which greatly reduces the polarization losses due to spin-lattice relaxation. As shown below, a signal enhancement factor over thermal polarization of about 1800 is achieved, allowing detection of a picomole quantity of analyte in a sample volume of 2.5  $\mu\text{l}$ , while maintaining the full resolution of conventional  $^1\text{H}$  NMR spectroscopy.

This is accomplished by letting the parahydrogen gas diffuse through a silicone elastomer membrane [61] to come into contact with a solution flowing through the chip at a constant rate. The solution contains a precursor, which is hydrogenated through a homogeneous catalyst also present in the solution. Two hydrogenative PHIP experiments are performed in this way. In the ALTADENA experiment, the solution is hydrogenated ‘on-chip’ at low magnetic field and transferred to a high field magnet for detection. ALTADENA was used as a proof of principle that the device was capable of hydrogenation ‘on-chip’. In the second experiment, PASADENA, the microfluidic device is held in the bore of a conventional NMR magnet using a purpose-built transmission line NMR probe. This yields a continuous on-chip stream of hyperpolarized material. As shown in the following, in addition to very high detection sensitivities, this also results in a continuous and highly stable operation of the system, making it possible to perform hyperpolarized two-dimensional NMR experiments [60, 62–64]. By replacing the hyperpolarized gas feed with hydrogen gas at thermal equilibrium, it is possible to gain kinetic information on the hydrogenation process, as well as to calibrate the intensity of the hyperpolarized NMR signals. This allows accurate assessment of the achieved polarization levels,

something that has been notoriously difficult in the context of parahydrogen-induced polarization.

## 1.3 Hyperpolarization

### 1.3.1 Sensitivity

As described in ??, NMR has low polarization levels that are governed by the Boltzmann distribution given in Eqn. ???. For example, for a spin-1/2 particle in a static field of 14.1 Tesla there is only a factor of  $6 \times 10^{-6}$  difference in the populations of the  $|\alpha\rangle$  and  $|\beta\rangle$  state. Compared to other detection techniques, NMR suffers from poor limits of detection (LODs). Raman Spectroscopy, has LODs of  $10^{-12} - 10^{-15}$  M, Laser induced fluorescence (LIF) has detected concentrations at  $10^{-13}$  M and mass spectrometry has achieved  $10^{-19}$  M. These alternative techniques are several orders of magnitude higher than that of NMR. While sensitivity is not a strong point, NMR is quantitative, non-invasive, and non-destructive making it an ideal tool for mass limited and, in particular, living samples.

### 1.3.2 Hyperpolarization

From Eqn. ?? in ??, we find that, the polarization level of nuclear spins at room temperature is low. In fact, for protons, it is only  $3 \times 10^{-6}$  per Tesla [65]. The signal derived from an NMR experiment is proportional to this polarization and means that the sensitivity and LOD is limited. The highest field available commercially is 28 Tesla which corresponds to polarization levels in protons of  $10^{-4}$  and whilst there are clear advantages to working in higher fields the size and more importantly - cost, make them unsuitable for many applications. Clearly just increasing the field is not a viable option if close to unity polarization is to be achieved.

There are techniques for increasing the spin polarization levels in samples to beyond the thermal equilibrium. The general term used to describe these is hyperpolarization. Hyperpolarization has applications in a diverse range of fields such as MRI [66–69], drug discovery [70, 71], reaction monitoring [72–74], metabolomics [75, 76], catalysis[77, 78] and material chemistry [79–81].

However, these hyperpolarized states are still subject to relaxation as discussed in ?? and return to thermal equilibrium with time constant  $T_1$ . This means the hyperpolarized spin order lasts seconds to minutes which limits their applications.

### 1.3.3 Techniques

#### 1.3.3.1 Brute Force

The most simple technique for hyperpolarization is "brute force". It is performed by simply cooling the sample to a few degrees kelvin in a high magnetic field [82, 83], under these circumstances, the polarization of  $^1\text{H}$  nuclei is 1%. In an experiment, the sample is first cooled to 2.3 K, after which, there is a waiting period to allow for the build up of polarization of the  $^1\text{H}$  nuclei. This period is required due to long  $T_1$  times at cryogenic temperatures and can be up to 70 hours [82]. After the polarization build up, the solid sample is passed through a low field to facilitate thermal mixing and polarization of  $^{13}\text{C}$  nuclei. Finally, the solid sample is rapidly dissolved in warm solvent and detected.

There are drawbacks however, firstly, the long  $T_1$  times at cryogenic temperatures mean long wait times are required in order to sufficiently build up polarization in the sample and prohibit high-throughput production. Secondly, and perhaps more importantly, the limit of polarization with this technique is around  $10^{-2}$  at achievable magnetic fields and temperatures.

#### 1.3.3.2 Dynamic Nuclear polarization

Dynamic nuclear polarization (DNP) methods use the thermal equilibrium electron spin polarization to polarize the nuclei under investigation. Close to unity polarization of the electrons is achieved by cooling to cryogenic temperatures (<2K) in a high magnetic field (>7 T). The electron polarization is transferred to nearby nuclear spins by saturating one of the transitions of the electron-nuclear coupled spin system with microwave frequency radiation.

The source of the electrons are 'free radicals' - molecules that have an unpaired electron spin, that are spread homogeneously throughout the sample. After cooling, the sample is held in a cryostat which is at 1.2 - 1.5K. The electrons have a much shorter  $T_1$  in contrast to nuclear spins so after irradiation with microwave radiation to induce polarization transfer between electrons and nuclei, the electrons repolarize quickly compared to the nuclei who retain non-equilibrium polarization. This polarization diffuses throughout the sample. After some time, tens of minutes is not uncommon, the nuclear spins are polarised to around 0.1 or 10%. The sample is then detected, either as the solid, or a liquid, depending on which type of DNP is being performed.

Several different types of DNP have been reported. These are solution state DNP [84], solid state magic angle spinning (MAS) DNP [85], rapid-melt DNP [86] and static solid state DNP with dissolution and observation [87]. The latter is most commonly referred to as dissolution-DNP and written as d-DNP.

The large equipment required for d-DNP, as well as the high cost of liquid helium for the cryostat and the extra superconducting magnet can make this method prohibitive for most NMR groups.

## 1.4 Parahydrogen Induced polarization - PHIP

### 1.4.1 Parahydrogen

Hydrogen exists as a diatomic made up of two protons and two electrons. As such, the total wave function contains electronic, vibrational, rotational and spin components and can be written as:

$$\Psi^{tot} = \Psi^{elec}\Psi^{vib}\Psi^{rot}\Psi^{spin} \quad (1.1)$$

Because the two protons are fermions they are subject to the Pauli exclusion principle which states that the total wave function must be antisymmetric with respect to exchange. With this in mind, it is important to note that the electronic, and vibrational states, are symmetrical in the ground state. and if we assume that they occupy the ground state, we find that the symmetry of the overall wave function depends of the symmetry of  $\Psi^{rot}\Psi^{spin}$ .

Rotational wavefunctions have quantum number  $J$ . For even numbers of  $J$  ( $J=0,2\dots$ ) the wavefunction is symmetric with respect to particle exchange for odd numbers of  $J$  ( $J=1,3\dots$ ) the wavefunction is antisymmetric. The nuclear spin wave function can also be symmetric or antisymmetric. By adding the angular momentum of both spins, it can be shown that they combine to give four possible quantum states with column vector representations derived from Eqn. ??:

$$|T^+\rangle = |\alpha\alpha\rangle = \begin{pmatrix} 1 \\ 0 \\ 0 \\ 0 \end{pmatrix} \quad (1.2)$$

$$|T^0\rangle = \frac{1}{\sqrt{2}} |\alpha\beta\rangle + |\beta\alpha\rangle = \frac{1}{\sqrt{2}} \begin{pmatrix} 0 \\ 1 \\ 1 \\ 0 \end{pmatrix} \quad (1.3)$$

$$|T^-\rangle = |\beta\beta\rangle = \begin{pmatrix} 0 \\ 0 \\ 0 \\ 1 \end{pmatrix} \quad (1.4)$$

$$|S^0\rangle = \frac{1}{\sqrt{2}} |\alpha\beta\rangle - |\beta\alpha\rangle = \frac{1}{\sqrt{2}} \begin{pmatrix} 0 \\ 1 \\ -1 \\ 0 \end{pmatrix}. \quad (1.5)$$

The three triplet ( $T$ ) states have spin quantum number  $I = 1$  and  $m_I = +1$ , 0, and -1 denoted by the superscript symbol on each state. The singlet ( $S$ ) state has  $I = 0$  and  $m_I = 0$ . The triplets states are symmetric with respect to spin exchange, whilst the singlet state is anti-symmetric with respect to spin exchange. Hydrogen in the triplet state is referred to as *ortho* and the singlet state is referred to as *para*.

In order for  $\Psi^{tot}$  to be antisymmetric, the antisymmetric rotational states are restricted to coupling to the symmetric (triplet) spin states whilst the symmetric rotational states are restricted to coupling to the antisymmetric (singlet) state.

The rotational energy is given by  $E_j = \frac{J(J+1)\hbar^2}{2I}$  where  $I$  is the moment of inertia of the diatomic and is given by  $I = \mu l^2$ , where  $\mu$  is the reduced mass, and  $l$  is the internuclear distance.

At room temperature, the ratio of *ortho* to *para* hydrogen is very nearly 3 to 1. However, by cooling down hydrogen the lowest ( $J = 0, 1$ ) rotational energy states start to become populated. The ratio of *para* to *ortho* hydrogen may be calculated using the respective partition functions [89]:

$$\frac{N_{\text{para}}}{N_{\text{ortho}}} = \frac{\sum_{J=\text{even}} (2J+1) \exp\left\{-\frac{J(J+1)\theta_R}{T}\right\}}{3 \sum_{J=\text{odd}} (2J+1) \exp\left\{-\frac{J(J+1)\theta_R}{T}\right\}}, \quad (1.6)$$

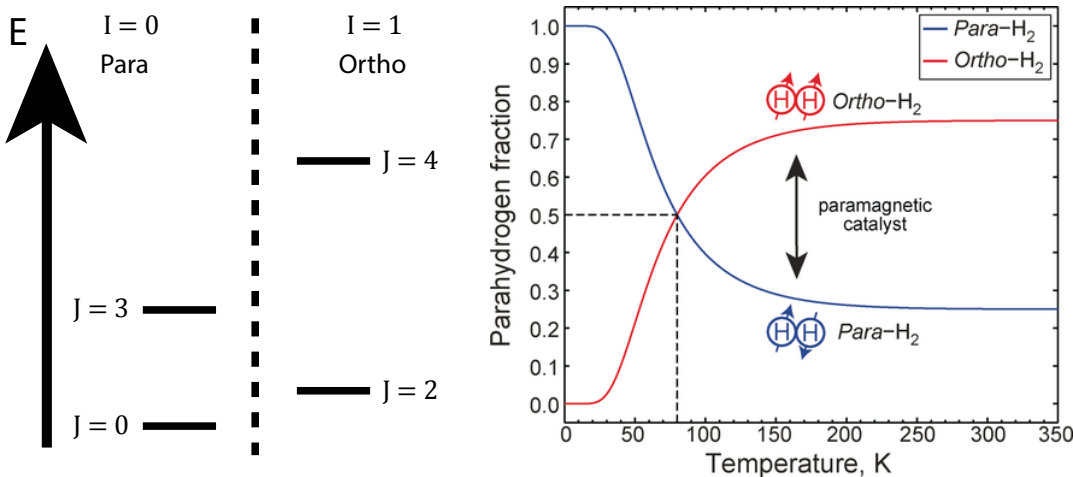


FIGURE 1.1: Left: The rotational energy levels of para- and orthohydrogen with their associated  $J$  values. Right: a graph showing the fraction of para- and orthohydrogen as a function of temperature. The dotted line shows 50% para enrichment that is achieved by cooling to 77K using liquid nitrogen. Image taken from [88].

for the first few levels this is:

$$\frac{N_{\text{para}}}{N_{\text{ortho}}} = \frac{1 + 5\exp\left\{-\frac{6\theta_R}{T}\right\} + 9\exp\left\{-\frac{20\theta_R}{T}\right\} + 13\exp\left\{-\frac{42\theta_R}{T}\right\} + \dots}{3(3\exp\left\{-\frac{2\theta_R}{T}\right\} + 7\exp\left\{-\frac{12\theta_R}{T}\right\} + 11\exp\left\{-\frac{30\theta_R}{T}\right\} + \dots)}, \quad (1.7)$$

where the rotational constant,  $\theta_R$ , is:

$$\theta_R = \frac{\hbar^2}{8\pi^2 I k_b}. \quad (1.8)$$

Using Eqn. 1.7, the percentage of parahydrogen in an equilibrium mixture can be plotted as a function of temperature, shown in Fig. 1.2.

By cooling alone, the ratio would remain unchanged. Conversion from ortho to para spin states without the aid of a catalyst (typically charcoal or iron (III) oxide) is not possible. The catalyst temporarily breaks the symmetry of the  $\text{H}_2$  molecule which allows spin-spin transitions and means a much larger fraction of the *para* form of hydrogen is produced. Crucially, when warmed up to room temperature in the absence of a symmetry breaking catalyst, no conversion from the singlet state  $|S^0\rangle$  back to the triplet states  $|T^+\rangle$ ,  $|T^0\rangle$ ,  $|T^-\rangle$  occurs. This is because transitions between singlet and triplet states are forbidden through quantum mechanical selection rules. It is therefore possible to store pure parahydrogen in the right container for days to weeks.

Para enrichment fraction,  $f$ , can be measured by NMR. By measuring the  $\text{oH}_2$  signal of the enriched  $\text{H}_2$  ( $S_e$ ) and comparing it to the signal obtained from the same amount of  $\text{H}_2$  at room temperature ( $S_{rt}$ ). The enrichment fraction is given by [90, 91]:

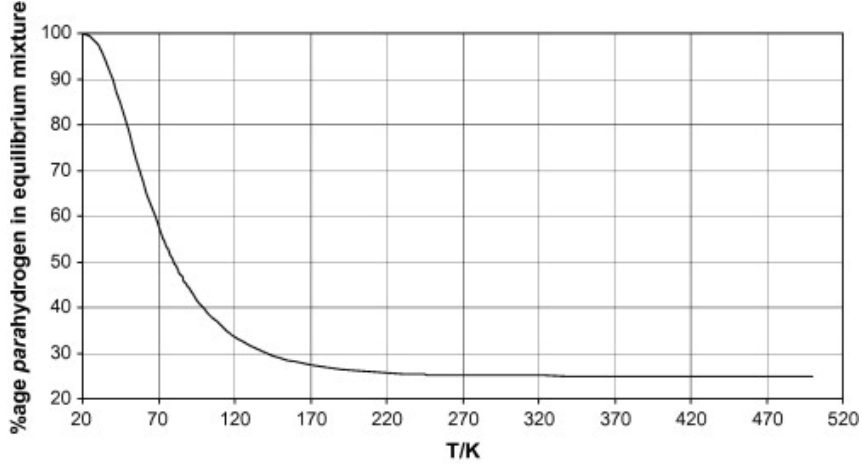


FIGURE 1.2: Calculated percentage of parahydrogen in an equilibrium mixture of *ortho*- and *parahydrogen* gas as a function of temperature using Eqn. 1.7 and  $\theta_R = 87.6$  K.  
Taken from [89].

$$f = 1 - (3S_e/4S_{rt}) \quad (1.9)$$

#### 1.4.2 PASADENA and ALTADENA

'Parahydrogen and synthesis allow dramatically enhanced nuclear alignment' (PASADENA)[92] and 'adiabatic longitudinal transport after dissociation engenders net alignment' (ALTADENA)[93] are subclasses of PHIP experiments characterised by the strength of magnetic field in which the hydrogenation and detection are performed.

The difference between PASADENA and ALTADENA are the  $J$ -coupling regimes in which the reaction and detection happens. The regime is determined by the value of the  $J$ -coupling (in Hz) compared to the value of the difference in chemical shifts of the individual protons. Where the strong regime has  $J$ -couplings that take the approximate value of the difference in chemical shift ( $\frac{\delta\omega}{J} \approx 1$ ), and the weak regime has  $J$ -couplings much smaller than the difference in chemical shift ( $\frac{\delta\omega}{J} \gg 1$ ). Since the chemical shift depends on external magnetic field ( $B_0$ ) and the  $J$ -couplings are independent of field one can select an appropriate magnetic field for the desired experiment. In PASADENA experiments the reaction and detection is carried out at high field ( $> 1$  T) whereas in ALTADENA the reaction is carried out at low field ( $< 10$  mT), and the product is transferred to a high magnetic field for detection[94].

This difference manifests itself as a difference in  $J$ -coupling regimes in the *parahydrogen* derived hydrogens in the product molecule. ALTADENA refers to hydrogens in the strong coupling regime upon addition and PASADENA refers to the weak coupling regime upon addition.

### 1.4.2.1 Spin Physics

The spin physics of PASADENA and ALTADENA can be interpreted through the density operator formulism. In a PASADENA type experiment, parahydrogen is added to a molecule in high field forming a weakly coupled AX system of the type discussed in 1.4.2. Due to the weak coupling,  $\frac{\delta\omega}{J} \gg 1$ , the eigenbasis is close to the Zeeman basis. The initial density operator,  $\hat{\rho}_{\text{ini}}$ , can be defined using Eqn. 1.2 as:

$$\hat{\rho}_{\text{ini}} = |S^0\rangle \langle S^0| = \frac{1}{2} |\alpha\beta - \beta\alpha\rangle \langle \alpha\beta - \beta\alpha|, \quad (1.10)$$

using the zeeman basis states for a 2 spins system from Eqn. 1.2 the matrix representation is:

$$\hat{\rho}_{\text{ini}} = \frac{1}{2} \begin{pmatrix} 0 \\ 1 \\ -1 \\ 0 \end{pmatrix} \otimes \begin{pmatrix} 0 & 1 & -1 & 0 \end{pmatrix} \quad (1.11)$$

$$= \frac{1}{2} \begin{pmatrix} 0 & 0 & 0 & 0 \\ 0 & 1 & -1 & 0 \\ 0 & -1 & 1 & 0 \\ 0 & 0 & 0 & 0 \end{pmatrix}. \quad (1.12)$$

This density operator may also be expressed as a linear combination of operators:

$$\rho_{\text{ini}} = \frac{1}{4} \mathbb{1} - \frac{1}{2} (2\hat{I}_{1x}\hat{I}_{2x} + \hat{I}_{1y}\hat{I}_{2y} + \hat{I}_{1z}\hat{I}_{2z}) \quad (1.13)$$

These diagonal elements (populations) do not evolve as these components commute with the Hamiltonian. The off-diagonal elements (coherences) evolve at a rate  $\approx \delta\omega$ .

The Hamiltonian of the product molecule is given by:

$$\hat{H}_{\text{pas}} = 2\pi(\omega_1\hat{I}_{1z}) + \omega_2\hat{I}_{2z} + 2\pi J_{12}(\hat{I}_{1x}\hat{I}_{2x} + \hat{I}_{1y}\hat{I}_{2y} + \hat{I}_{1z}\hat{I}_{2z}), \quad (1.14)$$

as the reaction continues, an ensemble of molecules are hydrogenated at different time points, this gives a new density operator,  $\hat{\rho}_{\text{pas}}(t)$ , expressed as:

$$\hat{\rho}_{\text{pas}}(t) = \exp\{-i\hat{H}_{\text{pas}}t\} \hat{\rho}_{\text{ini}} \exp\{+i\hat{H}_{\text{pas}}t\}. \quad (1.15)$$

Usually, the hydrogenation period is much longer than the coherence evolution. A new average density operator can be found by averaging the ensemble over the reaction time,  $t_r$  by:

$$\bar{\hat{\rho}}_{\text{pas}}(t_r) = \frac{1}{t_r} \int_{t=0}^{t_r} \hat{\rho}_{\text{pas}}(t) dt, \quad (1.16)$$

these coherences average to zero over the reaction time period and so the density operator becomes:

$$\hat{\rho}_{\text{pas}} = \frac{1}{2} \begin{pmatrix} 0 & 0 & 0 & 0 \\ 0 & 1 & 0 & 0 \\ 0 & 0 & 1 & 0 \\ 0 & 0 & 0 & 0 \end{pmatrix}, \quad (1.17)$$

and can also be written as:

$$\hat{\rho}_{\text{pas}}(t_r) = \frac{1}{4} \mathbb{1} - \hat{I}_{1z} \hat{I}_{2z} \quad (1.18)$$

Fig. 1.3 shows the eigenstate populations and general simulated spectra of a thermal equilibrium experiment and a PASADENA experiment.

In a usual NMR spectrum a  $\pi/2$  pulse is used to excite observable single quantum coherences. For a PASADENA signal to be observed, a  $\frac{\pi}{4}$  pulse must be used. The reason becomes clear when examining the effect on  $\hat{\rho}_{\text{pas}}(t_r)$  of a pulse with general tilt angle,  $\theta$ , along the  $y$ -axis:

$$\hat{R}(\theta)_y \hat{\rho}_{\text{pas}}(t_r) = \hat{\rho}_{\theta p} = \cos^2(\theta) \hat{I}_{1z} \hat{I}_{2z} + \cos(\theta) \sin(\theta) (\hat{I}_{1z} \hat{I}_{2x} + \hat{I}_{1x} \hat{I}_{2z}) + \sin^2(\theta) \hat{I}_{1x} \hat{I}_{2x}, \quad (1.19)$$

using a tilt angle of  $\theta = \pi/2$  would give:

$$\hat{\rho}_{\pi/2 p} = \hat{I}_{1x} \hat{I}_{2x}, \quad (1.20)$$

which is unobservable double quantum coherence. However, a pulse with  $\theta = \pi/4$  gives:

$$\hat{\rho}_{\pi/4 p} = \frac{1}{2} (\hat{I}_{1z} \hat{I}_{2z} + \hat{I}_{1z} \hat{I}_{2x} + \hat{I}_{1x} \hat{I}_{2z} + \hat{I}_{1x} \hat{I}_{2x}), \quad (1.21)$$

where the  $\hat{I}_{1x} \hat{I}_{2z}$  and  $\hat{I}_{1z} \hat{I}_{2x}$  terms are observable.

In an ALTADENA experiment, the hydrogenation is performed at low field. In this case, when a molecule of hydrogen is added to a substrate the density operator -  $\hat{\rho}_{\text{ini}}$ , is projected onto the new eigenbasis which at low field (where  $\frac{\delta\omega}{J} \ll 1$ ) is the singlet-triplet basis. To a good approximation the only term is the  $|S_0\rangle$  and there is no evolution of the system.

The sample is then transferred to high-field (where  $\frac{\delta\omega}{J} \gg 1$ ). It is done adiabatically, this means that the rate of change of magnetic field,  $dB_0/dt$  being small with respect to the value of the  $J$ -coupling between the protons, squared i.e.  $dB_0/dt < (J_{12})^2$ . As the field increases, the eigenbasis changes from singlet-triplet to the Zeeman basis. The adiabatic change carries the population of the  $|S_0\rangle$  state to the  $|\alpha\beta\rangle$  or  $|\beta\alpha\rangle$  state, depending on which is more energetically more favourable. This change is depicted graphically in Fig. 1.4 where  $|\beta\alpha\rangle$  has been arbitrarily chosen as the lower energy state. In the case shown, only one of the four energy levels, namely  $|\beta\alpha\rangle$  is now populated,

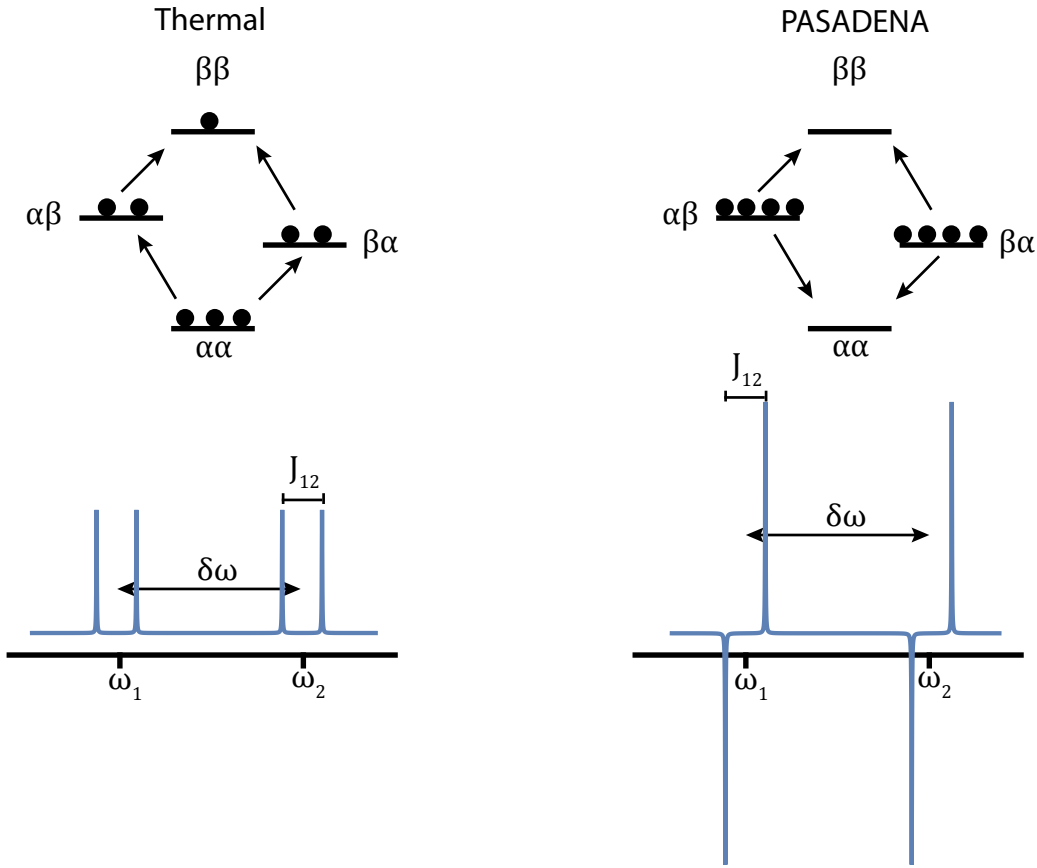


FIGURE 1.3: Above: Populations of states represented as balls in a thermal (left) and a PASADENA experiment. Below: Simulations of spectra arising from adding thermal hydrogen to a molecule (left) and of a PASADENA experiment when adding parahydrogen.

therefore the density operator,  $\hat{\rho}_{alta}$  is given by:

$$\hat{\rho}_{alta} = |\beta\alpha\rangle \langle \beta\alpha|. \quad (1.22)$$

This leads to [93]:

$$\hat{\rho}_{alta} = \hat{I}_{1z}\hat{I}_{2z} \pm \frac{1}{2}(\hat{I}_{1z} - \hat{I}_{2z}), \quad (1.23)$$

where the positive sign applies if  $J_{12}(\omega_1 - \omega_2) < 0$ , and the negative sign applies in the opposite case.

An r.f. pulse with general angle,  $\theta$ , orientated along the  $y$ -axis gives:

$$\hat{R}(\theta)_y \hat{\rho}_{alta} = \hat{\rho}_{\theta a} = \cos(\theta) \sin \theta (\hat{I}_{1z}\hat{I}_{2x} + \hat{I}_{1x}\hat{I}_{2z}) \pm \frac{1}{2} \sin \theta (\hat{I}_{1x} - \hat{I}_{2x}). \quad (1.24)$$

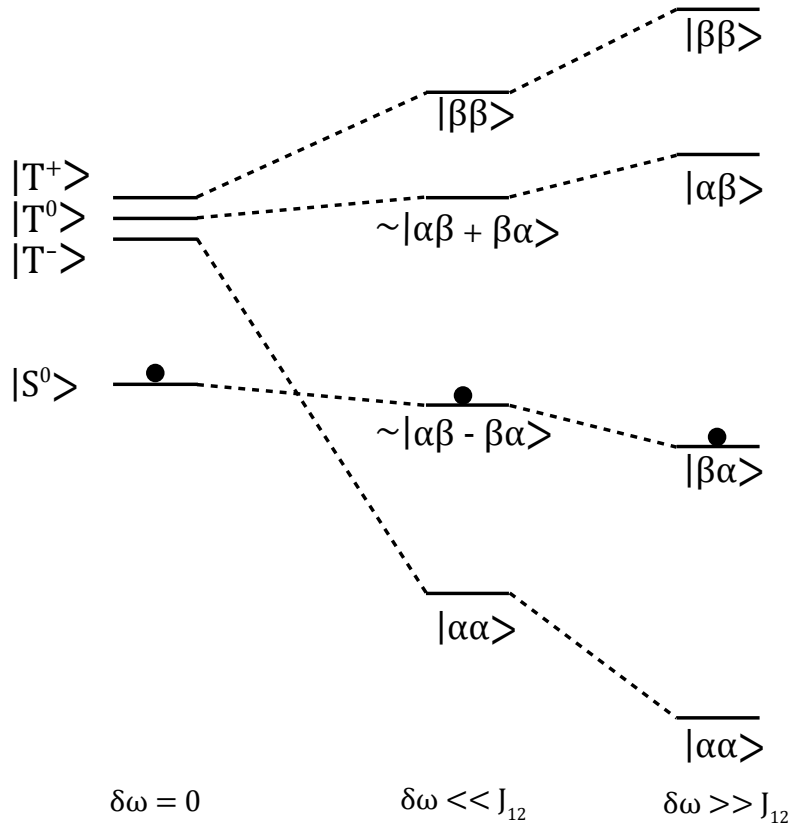


FIGURE 1.4: Correlation diagram for the ALTADENA effect. Hydrogenation at low field populates the singlet state, adiabatically increasing the field carries the population into a high field state.

A pulse with  $\theta = \pi/4$  here yields:

$$\hat{\rho}_{\pi/4a} = \frac{1}{2}(\hat{I}_{1z}\hat{I}_{2x} + \hat{I}_{1x}\hat{I}_{2z}) \pm \frac{1}{2\sqrt{2}}(\hat{I}_{1x} - \hat{I}_{2x}), \quad (1.25)$$

that gives rise to two out of phase doublets shown in Fig. 1.5. However, unlike PASADENA, ALTADENA does not require a  $\pi/4$  pulse so  $\pi/2$  pulses are more common.

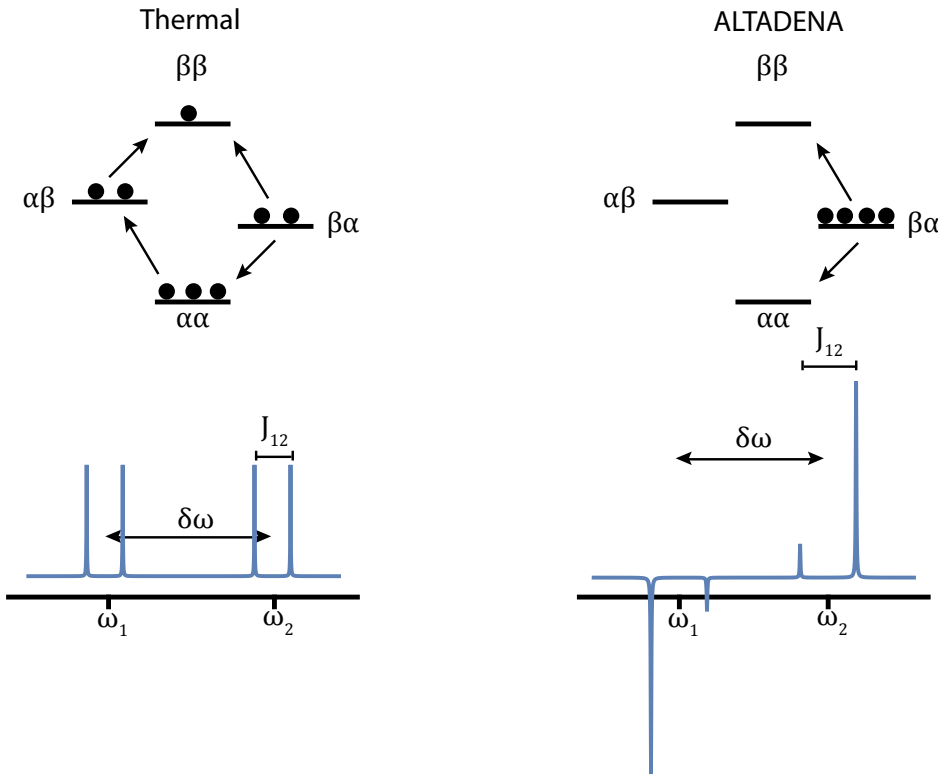


FIGURE 1.5: Top: Populations of Zeeman states represented by balls for thermal(left) and ALTADENA(right) experiments. Bottom: Simulations of a thermal spectrum after applying a  $\pi/4$  pulse and an ALTADENA experiment.

## 1.5 Materials and methods

The microfluidic chips for the PASADENA experiments were constructed from three layers of cell cast PMMA sheet material (Weatherall Equipment). The sheet thickness was 200  $\mu\text{m}$  for the top and bottom layers, and 500  $\mu\text{m}$  for the middle layer. The fluid and gas channels were designed on AutoCAD and cut into the PMMA using a laser cutter (HPC Laser L3040) to a width and depth of 150  $\mu\text{m}$ . The layers were subsequently bonded together with a plasticiser (2.5% v/v dibutyl phthalate in isopropyl alcohol) under heat and pressure (358 K, 3.5 tonnes) [95]. The total internal fluid volume is 4  $\mu\text{l}$ , and the sample chamber is 2.5  $\mu\text{l}$ .

The chip for the ALTADENA experiment was a single 500  $\mu\text{m}$  layer of PMMA. The fluid and gas channels for this device were designed and cut in the same manner as above.

Both devices also employ a poly(dimethyl siloxane) (PDMS) membrane (Shielding Solutions) to facilitate para-H<sub>2</sub> transport, of 1 mm thickness with laser-cut screw holes. The parahydrogen polarization lifetime in the PDMS after O<sub>2</sub> removal was measured to be  $\sim 4$  h.

The PMMA chips and PDMS membrane layer are sealed with a pair of screw-tightened 3D printed (Accura Xtreme, Proto Labs) holders, with fluid and gas in/out ports (to fit Kinesis UK NanoPorts).

For PASADENA experiments, the assembled microfluidic device was put in a transmission line based home-built probe [96]. The device sits between the two stripline planes on a sample holder having sample chamber of the device coinciding with the constriction on stripline planes. PASADENA and 2D NMR experiments were performed at a field strength of 11.7 T with an AVANCE III console. Nutation frequencies for RF pulses were 100 kHz for protons, and 20 kHz for carbon in the case of the HMQC spectrum. 16k data points were acquired over 1.2 s for proton 1D spectra. Saturation recovery experiments used a train of 512  $\pi/2$  pulses separated by a delay of 0.1 ms, followed by a recovery delay, and a  $\pi/4$  excitation pulse. The PH-TOCSY spectrum was acquired using the States-TPPI method, with 256  $t_1$  increments, averaging 8 transients per increment. 2048 complex data points in 0.2 s were acquired for each increment. The PH-HMQC experiment was acquired using the States method, with 128  $t_1$  increments, averaging 8 transients with 2048 complex points over 0.2 s. 1D spectra and 2D spectra were processed using scripts written in Julia [97].

For ALTADENA experiments, the device was placed outside the magnet in order for the hydrogenation to occur at low field. The solution was passed through the device and into a 5 mm NMR tube (NORELL). ALTADENA NMR experiments were performed at a field strength of 16.5 T with a NEO console with cryoprobe. The 1D spectra were processed also using scripts written in Julia [97].

To generate parahydrogen gas at 50% para enrichment, hydrogen gas (purity 99.995%) was passed through a home-built parahydrogen generator containing an iron (III) oxide catalyst cooled to 77 K using liquid nitrogen.

The solution before both experiments contained 20 mM propargyl acetate **2** and 5 mM 1,4-bis(diphenylphosphino)butane(1,5-cyclooctadiene)rhodium tetrafluoroborate **3** in methanol-d<sub>4</sub>. In an attempt to avoid possible spin relaxation or chemical side-reaction effects, dissolved oxygen from the atmosphere was removed by 5 minutes of vigorous helium bubbling.

The parahydrogen gas was delivered through a PTFE tube (1/16 inch O.D., 1/32 inch I.D.) into the 3D printed chip holder, and out via a second PTFE line, using a mass flow controller (Cole-Parmer) to limit the flow to 20 ml min<sup>-1</sup> at an overpressure of 5 bar. Although most of the parahydrogen gas passes directly through the system, some amount dissolves into the PDMS layer, which in terms of H<sub>2</sub> solubility behaves similarly to other organic solvents. The solution was loaded into a 3.5 ml plastic syringe with a Luer lock connection to in-flow PEEK tubing (1/16 inch O.D., 0.007 inch I.D.) leading to the chip. The same tubing was used for the solution out-flow into a container exposed to

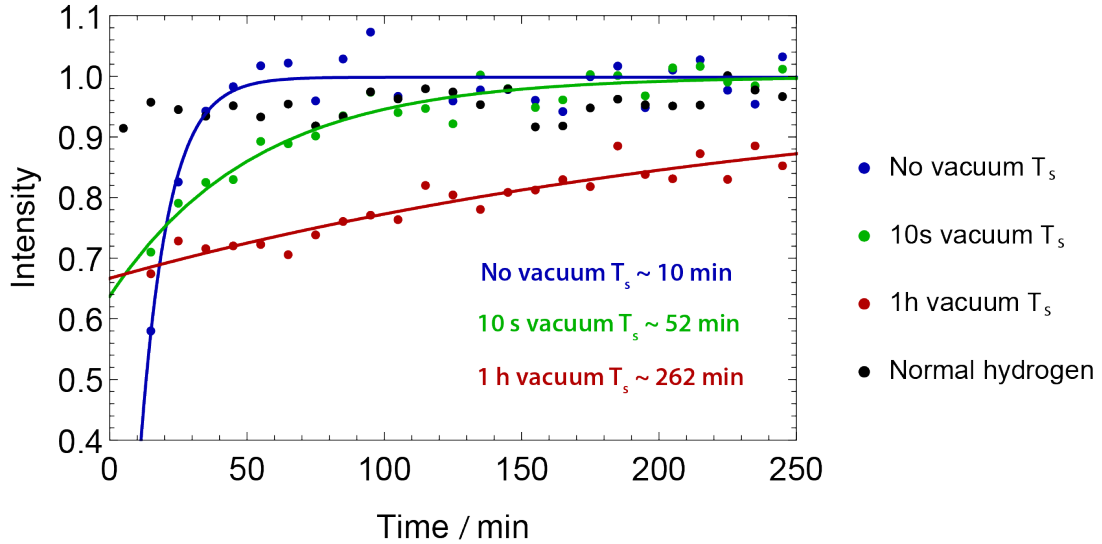


FIGURE 1.6: Ortho-para conversion of hydrogen in PDMS after various times under vacuum.

a back pressure of 1.5 bar of nitrogen gas, to preventing formation of hydrogen bubbles in the chip. Solution flow into the chip was controlled with a syringe pump (Cole-Parmer).

## 1.6 Results and Discussion

### 1.6.1 Parahydrogen relaxation in PDMS

To determine the hydrogen ortho-para conversion in PDMS, the ortho-para conversion time of H<sub>2</sub> dissolved in PDMS was measured. A high-pressure NMR tube of 5 mm outer diameter (Sigma-Aldrich) was filled with PDMS resin (Sylgard 84, 3M). A teflon capillary of 1/16 inch outer diameter (Sigma-Aldrich) was pushed into the NMR tube along the central axis, and the PDMS was allowed to cure. The capillary was then removed, leaving a cylindrical void in the centre of the NMR tube. The tube was then exposed to vacuum for varying amounts of time, in order to study the conversion effect of the residual oxygen the results of which are shown in Fig. 1.6.

The detectable thermal signal in the ortho-para conversion experiment is given by  $(1 - \frac{1}{3}(4f - 1))$ , where  $f$  is the para-enrichment level of the H<sub>2</sub> gas. Therefore, the equilibrium ratio of  $f = 0.25$  gives a signal of 1, and pure parahydrogen gas gives no signal. Hence, our signal starting at 50% enrichment should vary from 2/3 to 1. The data was fit to a function of the form  $(A - B e^{-\frac{t}{T_s}})$ , with A, B and T<sub>s</sub> as variables. The T<sub>s</sub> under no vacuum of 10 min lead to the assumption that no significant relaxation would occur during the transport of H<sub>2</sub> through the PDMS membrane.

### 1.6.2 Reaction Scheme

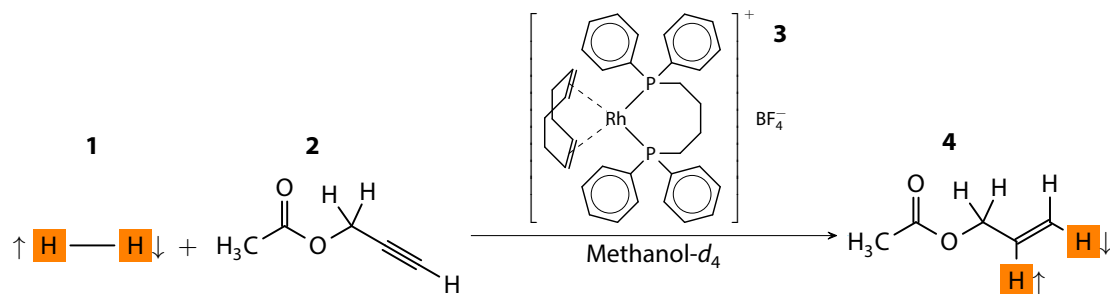


FIGURE 1.7: Scheme of the reaction used in the PHIP@chip experiment. Hydrogen gas **1** enriched in parahydrogen reacts with propargyl acetate **2** in the presence of the Rh catalyst **3** to form allyl acetate **4**.

The hydrogenation reaction system employed in the present work is shown in Fig. 1.7. Parahydrogen-enriched hydrogen gas **1** was allowed to react with propargyl acetate **2**, in the presence of a rhodium catalyst **3**. The substrate **2** was chosen in view of future studies based on side-arm hydrogenation (SAH) [57, 58, 98]. In SAH the polarisation of the <sup>1</sup>H nucleus is transferred to a neighbouring <sup>13</sup>C and the moiety that has been hydrogenated is removed. SAH techniques can help to bring generality to the PHIP technique as they eliminate the need for the hyperpolarized target molecule to contact unsaturated bonds.

### 1.6.3 ALTADENA

In order to verify that the parahydrogen transfer on chip was possible, an experiment was performed whereby the parahydrogen transfer was microfluidic and ‘on chip’ but the detection was performed in a conventional NMR tube and probe.

This ALTADENA type experiment involved the addition of para enriched hydrogen gas to propargyl acetate outside the magnetic field in a device shown in Fig. 1.8. This device is a simpler version of the one eventually used. It features 3D printed holders that are used to deliver the gas and liquid as well as seal against any liquid or gas leak. The chip is made from a single 500  $\mu\text{m}$  thick layer of PMMA with serpentine paths for liquid and gas flow. B in the Fig. 1.8 shows the path structure in the chip as well as the hydrogen and fluid paths respectively.

The set-up for this experiment employs a syringe pump, the hydrogenation device outside the magnet and a standard 5 mm NMR tube inside the 16.5 T magnet. The device was pressurised with 5 bar of 50% enriched parahydrogen and allowed to equilibrate for some time. Then, 100  $\mu\text{l}$  was flown through the device at a flow rate of 1000  $\mu\text{l min}^{-1}$  this was done to ensure the sample from the experiment would reside completely in the sensitive area. For the ALTADENA, 350  $\mu\text{l}$  was flown through the device and collected in the

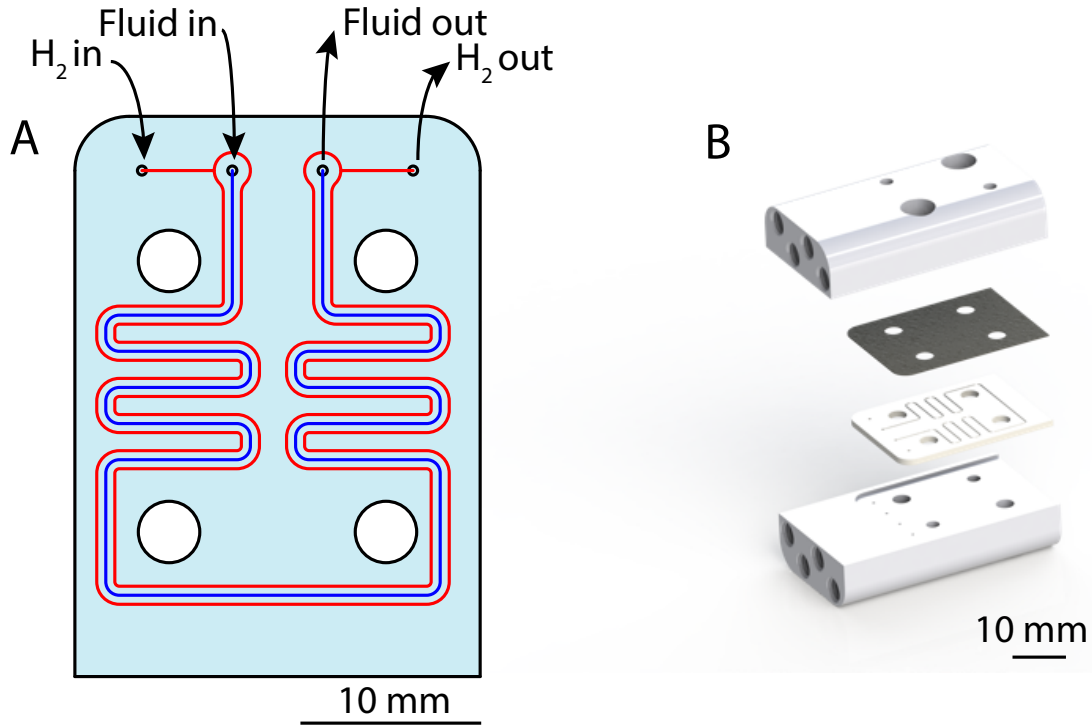


FIGURE 1.8: A) Liquid channel (blue) and hydrogen channel (red) as scored onto the PMMA layer of the device. B) A 3D render of the hydrogenation device used for the ALTADENA experiments.

magnet. A  $\pi/4$  pulse was applied and the spectra recorded the result of the experiment is shown in Fig. 1.9.

A comparison is shown between scans taken of the same experiment, in Fig. 1.9 i) spectra from an experiment with thermal hydrogen and ii) one with parahydrogen. The parahydrogen ALTADENA signal (ii) exhibits the characteristic inverted peaks and a much higher signal to noise ratio (SNR) and gives enhancement by comparison of the SNR of around 200. This result provided a proof of principle that parahydrogenation induced polarization (PHIP) on a chip was possible by bubble free transfer through a PDMS membrane in our devices.

#### 1.6.4 PASADENA

Fig. 1.10 shows the microfluidic device used for the present study. It consists of a chip made from PMMA, which houses a sample chamber of 2.5 L volume that aligns with the transmission line detector of a home-built NMR probe assembly, which was fitted inside of an 11.7 T NMR magnet. Fluid is flowed through the chip by means of a syringe pump installed outside of the magnet bore; connections are made through threaded ports in the two 3D-printed holders shown in Fig. 1.10b. Para-enriched H<sub>2</sub> gas at 5 bar

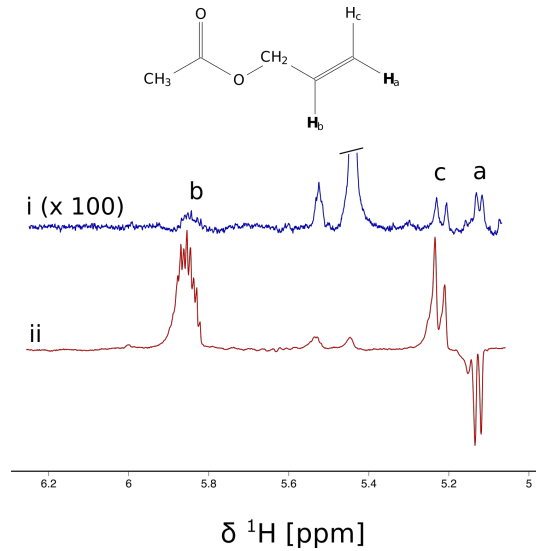


FIGURE 1.9: Spectra obtained from i) a thermal hydrogenation and ii) a parahydrogenation of propargyl acetate to give allyl acetate with hydrogens derived from parahydrogen labelled a and b. By comparison of SNR the enhancement for the ALTADENA experiment is 200.

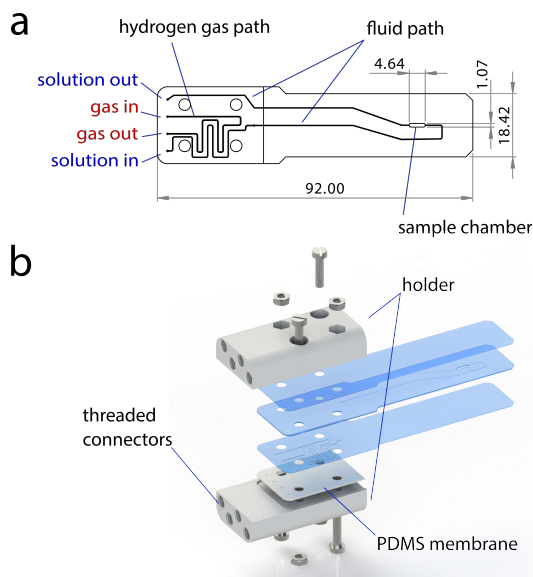


FIGURE 1.10: Overview of the PHIP@chip device. a: outline drawing of the chip (dimensions in mm). b: CAD rendering of the chip assembly with individual chip layers separated, consisting of the PMMA chip, PDMS membrane, and two 3D printed holders with threads for the gas and fluid connections. The hydrogen gas diffuses through the PDMS membrane into the flowing liquid.

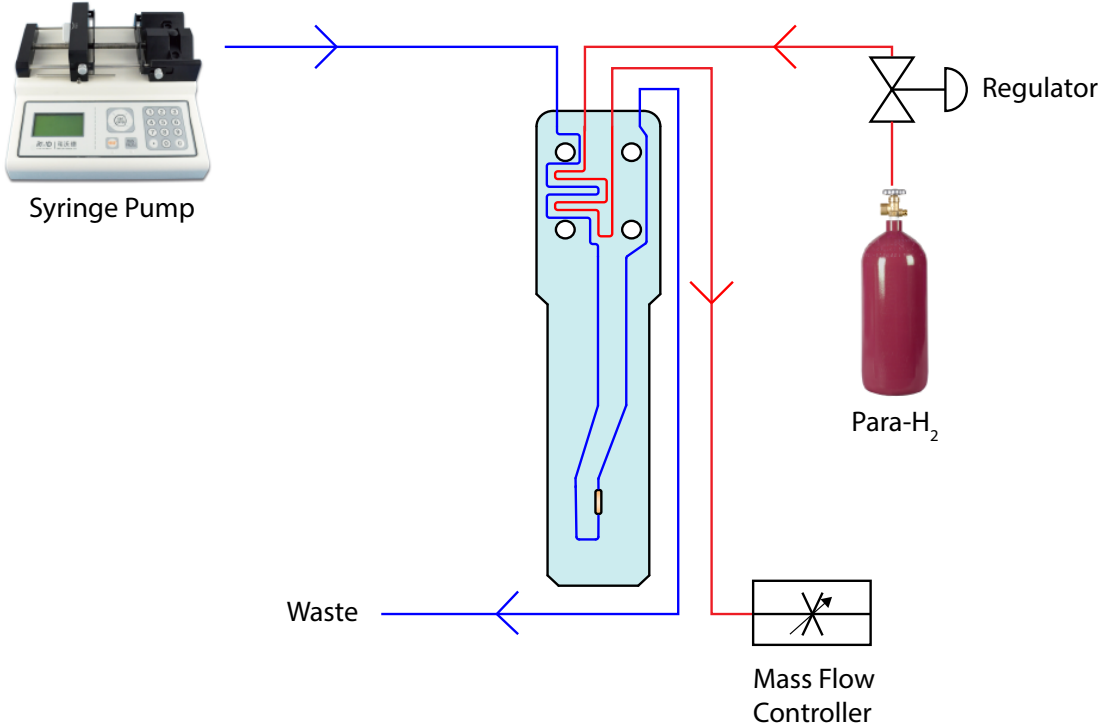


FIGURE 1.11: Drawing of PHIP@chip setup. It shows the solution (blue line) of propargyl acetate, catalyst and methanol being fed into the magnet via a syringe pump. Simultaneously, parahydrogen (red line) is fed in at the desired pressure and regulated by a mass flow controller to a flow rate of  $20 \text{ mlmin}^{-1}$ . Both of these are fed into the microfluidic device depicted in Fig. 1.10

above ambient pressure flows through a second channel in the chip, which runs in the immediate vicinity of the liquid channel. A depiction of the set-up is given in Fig. 1.11.

The chip consists of three laser-cut layers of poly methylmethacrylate (PMMA) bonded together, as shown in Fig. 1.10b. Channels in the left part of the chip, where it is clamped between the holders, are cut through the top layer, while they are scored into the middle layer of the chip (and hence sealed from the outside) in the free part of the device. Within the clamps, the exposed channels are sealed by means of a PDMS membrane. The flowing liquid as well as the pressurised hydrogen gas are therefore exposed to the PDMS layer, which serves as a diffusion bridge for the hydrogen. The holders, made by 3D printing, keeps the membrane and the chip aligned, and maintains mechanical pressure to ensure sealing. Channels inside the holders guide the fluid and gas to and from the four access points at the top end of the chip, as shown in Fig. 1.10b. The PDMS membrane acts both as a diffusion conduit for hydrogen gas and as a fluid seal. In a crucial difference to the otherwise similar geometry of the hydrogenation chip used by Bordoni et al[99], the gas and liquid channels are arranged side by side, and molecular hydrogen diffuses through the bulk of the PDMS membrane rather than across the membrane. Clamping the PDMS membrane onto the chip using the holders, makes it possible to use large gas pressures (up to 5 bar in the present experiments).

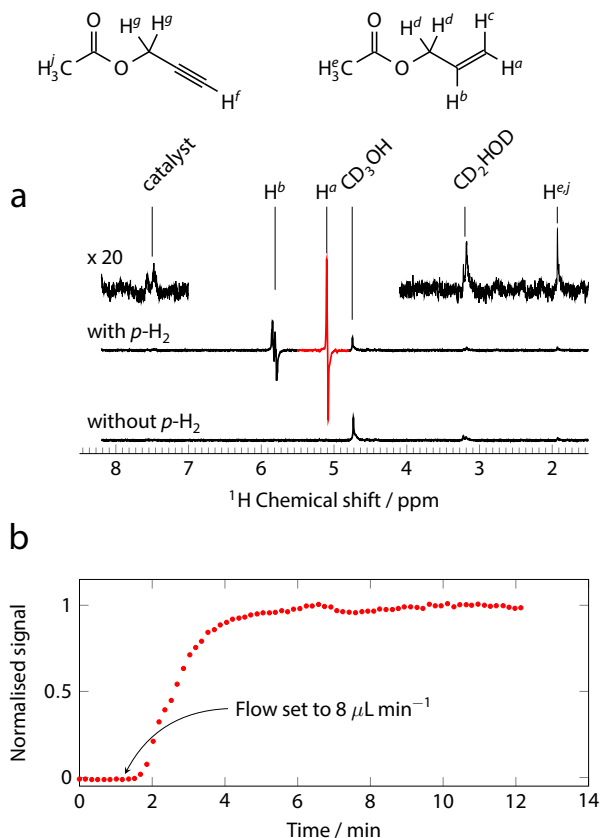


FIGURE 1.12: a: Single-scan proton NMR spectrum obtained with parahydrogen at 5 bar using the PHIP@chip setup at a continuous flow rate of  $8 \mu\text{L min}^{-1}$  (top trace with enlargement). Antiphase doublets from the two hyperpolarized protons  $\text{H}^a$  and  $\text{H}^b$  are clearly visible at 5.17 ppm and 5.92 ppm, respectively. Without parahydrogen, these signals are not observed (bottom trace). b: Buildup of the hyperpolarized signal ( $\text{H}^a$ ) after initiation of flow.

This would be difficult to achieve in the chip presented by Bordonali et al, which has the liquid and gas channels arranged on opposite sides of the membrane.

### 1.6.5 Signal Analysis

Fig. 1.12a shows a single-scan proton NMR spectrum obtained from a steady-state PHIP@chip experiment (top trace), compared to the spectrum obtained without parahydrogen (bottom trace). The hyperpolarized spectrum is dominated by an antiphase doublet, centred at 5.17 ppm, and an antiphase multiplet at 5.92 ppm, corresponding to protons in the  $\text{H}^a$  and  $\text{H}^b$  positions of the hydrogenation product **4**. The PDMS membrane is equilibrated with para-enriched hydrogen gas, which is supplied from an aluminium storage tank at a regulated pressure of 5 bar. The gas flow rate is kept constant at  $20 \text{ mL min}^{-1}$  by means of a mass flow controller placed after the chip. This ensures that the gas channel always contains fresh para-enriched hydrogen gas at the design pressure of 5 bar. The fluid channel of the chip is pre-filled with a solution of 20 mM precursor **2** and 5 mM catalyst **3** in methanol-*d*<sub>4</sub>. NMR spectra are acquired

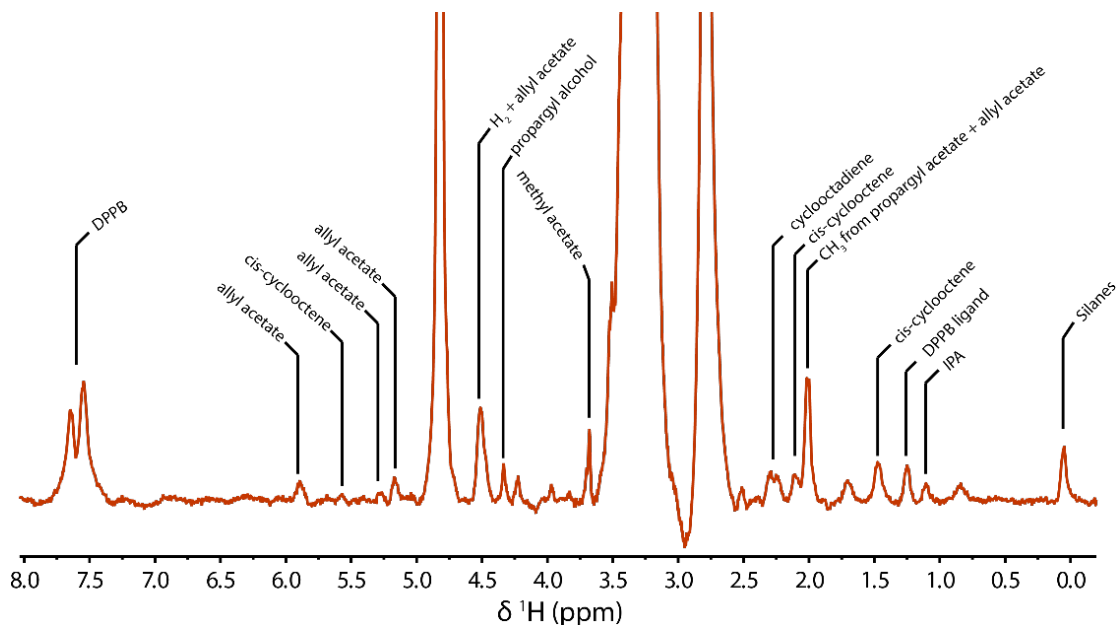


FIGURE 1.13: Labelled  $^1\text{H}$  spectrum acquired using a flow rate of  $2\mu \text{ lmin}^{-1}$  and a normal hydrogen pressure of 5 bar. The spectrum was collected using 64 transients with a delay of 5 seconds.

every 30 s, using a  $\pi/4$  excitation pulse. The fluid channel is connected to a syringe pump situated outside the NMR magnet. The liquid flow is started by setting the target flow rate on the syringe pump to  $8 \text{ L min}^{-1}$  (marked by an arrow Fig. 1.12b). The NMR signal intensity begins to rise about 30 s later, and reaches a steady state after about two minutes.

Using normal hydrogen gas, a fully labelled spectrum of the reaction mixture was obtained using a lower flow rates whilst maintaining the 5 bar of hydrogen pressure. This allowed the solution to saturate with methanol and facilitated the quantification of the product and dissolved hydrogen. A fully labelled spectrum obtained using a flow rate of  $2\mu \text{ lmin}^{-1}$  is shown in Fig. 1.13

### 1.6.6 Hydrogen Transport

The hydrogen transport through the membrane and its uptake into the flowing liquid was simulated using two coupled finite element models: a dilute species diffusion model for hydrogen gas in the PDMS membrane, and a dilute species diffusion and convection model for hydrogen dissolved in the flowing liquid. The hydrogen partial pressures at the liquid/PMDS interface are constrained to be equal, and the hydrogen partial pressure at the gas/PDMS interface was set to a fixed value of 5 bar. Fig. 1.14a shows the diffusive flux of hydrogen through the PDMS membrane. Since the gas/PDMS interface acts as a source, and the liquid/PMDS interface as a sink for hydrogen, the flux is strongest where the two channels are in close proximity. At the lowest flow rate,

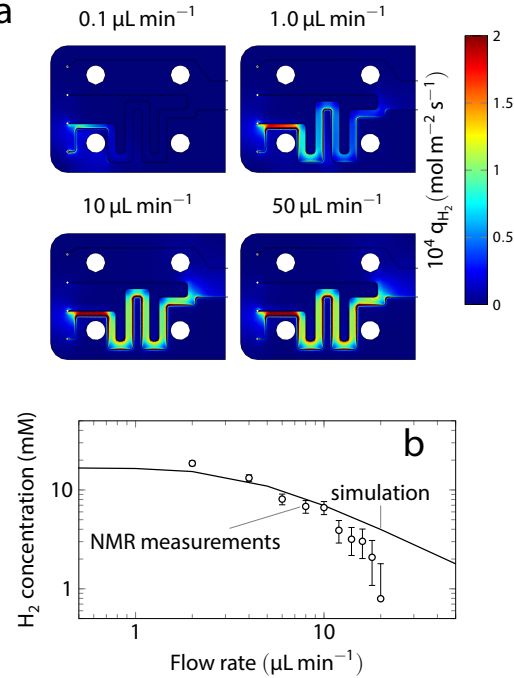


FIGURE 1.14: Finite element simulation of hydrogen uptake. a: Diffusive hydrogen flux in the PDMS membrane for different liquid flow rates; b: final hydrogen concentration in flowing methanol as a function of flow rate. Solid line: simulation, open circles: NMR measurements.

significant transport only takes place in a very small area, and the liquid is saturated with hydrogen within the first few mm of the path which is in contact with the PDMS. The higher the flow rate, the further the area of significant flux extends downstream. At about  $10 \text{ l min}^{-1}$ , the hydrogen flux covers the entire length of the area between the liquid and gas channel interfaces. The finite element model also predicts the resulting concentration of hydrogen in the liquid (methanol) as a function of flow rate. This is shown by the solid line in Fig. 1.14b. The circles represent NMR measurements. At flow rates between  $2$  and  $10 \text{ l min}^{-1}$ , experimental results are in good agreement with the simulation. At higher flow rates, however, the experimentally observed hydrogen concentrations are significantly lower than the predictions. It is currently unclear what causes this discrepancy; possibly high flow rates lead to deformation of the PDMS layer over the liquid channel and thus change the uptake geometry. At flow rates below  $10 \text{ l min}^{-1}$ , the simulation and experiments both indicate that the flowing solvent is nearly saturated with hydrogen.

### 1.6.7 Sensitivity and Limit of Detection

Clearly, the steady-state signals observed at constant flow rate are the result of a dynamic equilibrium between the rate of hydrogenation, the rate of transport of the hydrogenated product to the sample chamber and its removal from it, and spin-lattice relaxation.

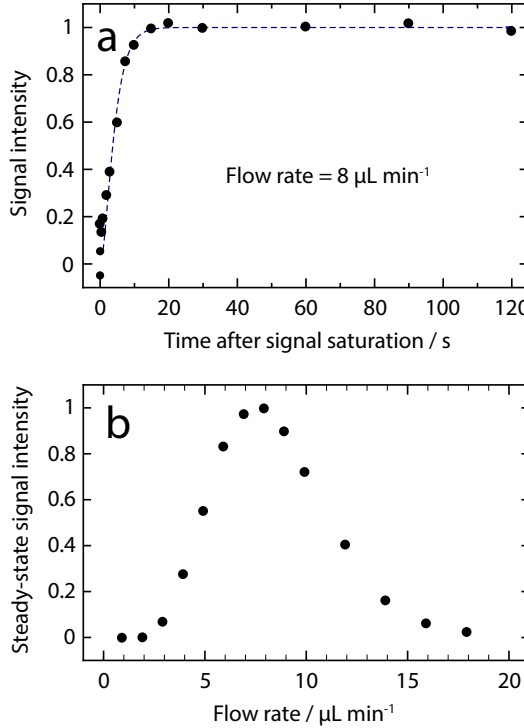


FIGURE 1.15: Saturation recovery results. a: Signal buildup at constant flow rate after saturation (solid dots: measured data points, the dashed line is a guide to the eye); b: Magnitude of the steady-state signal after full recovery (at least 100 s after saturation) as a function of flow rate. A clear maximum at  $8 \mu\text{L min}^{-1}$  is observed.

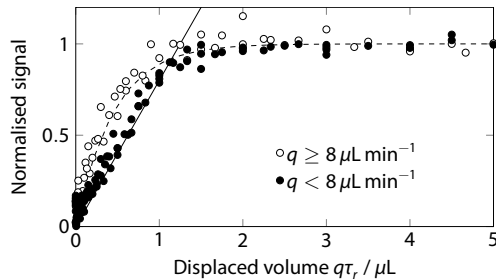


FIGURE 1.16: Signal recovery after saturation, normalised by the maximum signal observed at long recovery times. The horizontal axis is the volume moved through the chip during the recovery time  $\tau_r$ , i.e.,  $q\tau_r$ , where  $q$  is the flow rate. Filled circles correspond to flow rates below the optimum ( $q < 8 \mu\text{L min}^{-1}$ ), whereas open circles are obtained at flow rates  $q \geq 8 \mu\text{L min}^{-1}$ . The solid and dashed lines are guides to the eye for the solid and open circle data points, respectively.

In order to probe the interplay of these factors, the NMR signal was suppressed by saturating the spin populations with a train of 512  $\pi/2$  pulses separated by 100  $\mu\text{s}$  delays. The signal intensity was then measured as a function of the delay between the end of the saturation train and the NMR excitation pulse. Fig. 1.15a shows an example of the data thus obtained at a flow rate  $q = 8 \text{ L min}^{-1}$ . The signal increases rapidly after saturation, reaching steady-state levels after about 10 s.

The intensity of the steady-state NMR signal exhibits a clear maximum with flow rate

(Fig. 1.15b), reflecting a balance between hydrogen uptake, reaction kinetics, and spin-lattice relaxation. The optimum, with the largest signal at saturation, is reached at a flow rate of  $8 \text{ L min}^{-1}$ . The nature of the stationary state established in the system at each flow rate becomes clearer if the saturation recovery data is plotted in terms of the volume displaced during the saturation recovery time  $q\tau$ , rather than the recovery time itself, and normalised to the steady-state signal intensity at each flow rate, as shown in Fig. 1.16. At flow rates below the intensity maximum at  $q < 8 \text{ L min}^{-1}$  (solid circles), the data points collapse onto a curve that shows an initial linear increase up to a displaced volume of about  $1 \mu\text{L}$ , followed by rapid saturation to the steady-state value. This behaviour clearly indicates that the signal recovery in this regime is dominated by the convective fluid transport. At these flow rates, a constant concentration of hyperpolarized material is established in the flowing liquid upstream of the sample chamber, and is simply carried back into view of the NMR detector after the saturation pulses end. The maximum signal is reached after a volume of about  $1.5 \mu\text{L}$  has been displaced. This is less than the capacity of the sample chamber, reflecting the uneven velocity distribution inside it. At flow rates above the optimum ( $q \geq 8 \text{ L min}^{-1}$ ), a somewhat different behaviour is observed. The initial recovery rate is faster (Fig. 1.16, open circles), and appears to follow an exponential rather than linear shape. This suggests that at these flow rates, the stationary state is not yet established at the point where the liquid enters the sample chamber, and therefore, the observed recovery is dominated by the ongoing hydrogenation reaction.

In order to determine the sensitivity of detection of the hydrogenation product at the optimum flow rate, the experiment was repeated using normal hydrogen. In this case, the signal from protons  $\text{H}^a$  and  $\text{H}^b$  of the hydrogenation product **4** are too weak to be observed above the noise in a single scan. Fig. 1.17 compares the hyperpolarized signal (a) to the averaged signal of 512 transients obtained with hydrogen in thermal equilibrium (b).

Since the methyl group in the precursor and the hydrogenation product contribute to the same signal at 2.05 ppm (signal labelled  $\text{H}^{e,j}$  in Fig. 1.12a), this signal can be used as a calibration standard, with a concentration of 20 mM which is unaffected by the hydrogenation reaction. By comparing this integral to that of the signal from the  $\text{H}^a$  protons, the concentration of hydrogenated product can be quantified. At a flow rate of  $8 \text{ L min}^{-1}$ , an allyl acetate (product) concentration of  $(0.29 \pm 0.05) \text{ mM}$  was found, corresponding to a total of  $(0.725 \pm 0.125) \text{ nmol}$  in the  $2.5 \text{ L}$  sample volume.

This quantity can be used to determine the limit of detection of the hyperpolarized product. The signal/noise ratio (SNR) in the spectrum shown in Fig. 1.17a is  $400(\pm 10\%)$ , and the line width is  $6 \pm 0.5 \text{ Hz}$ . The normalised limit of detection is given by Eqn. ??

$$\text{nLOD}_\omega = \frac{3n}{\text{SNR} \sqrt{\Delta f}},$$

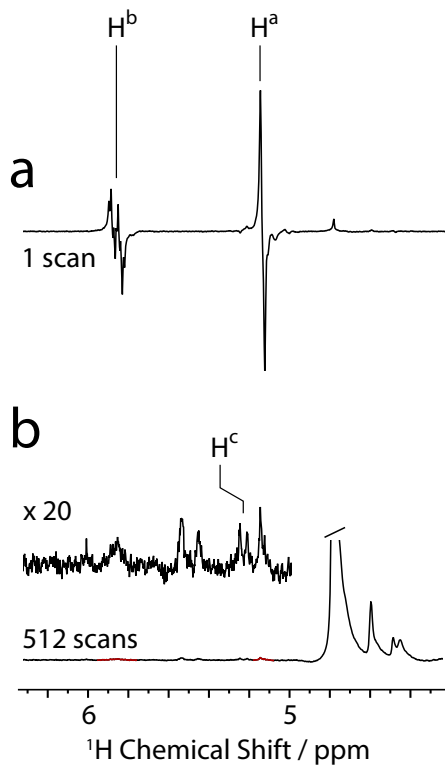


FIGURE 1.17: a: Single-scan steady-state spectrum obtained at the optimum flow rate with para-enriched  $\text{H}_2$ ; b: spectrum obtained at the same flow rate with hydrogen gas in thermal equilibrium. 512 transients have been averaged. Signal enhancement by PHIP was determined by comparing the integral of the positive lobe of the  $H^a$  signal in spectrum a to the integral of the corresponding (purely absorptive) peak in spectrum b.

where  $n$  is the amount of sample and  $\Delta f$  is the signal bandwidth. In the present case, one finds  $n\text{LOD}_\omega = (2.2 \pm 0.4) \text{ pmol } \sqrt{s}$ . Limits of detection in this range have so far only been reported in very limited circumstances, including chemically-induced dynamic nuclear polarization (CIDNP) [100], or by making use of unconventional low-field detection systems such as force-detected magnetic resonance or optical detection methods[28–38]. In the present case, we are using conventional inductive detection, and retain the full resolution and specificity that make high-field analytical tool.

The mass limit of detection (LOD) for protons at a magnetic field of 14.1 T (corresponding to a proton Larmor frequency of 600 MHz) in state-of-the-art commercial NMR probes with a conventional sample volume of 0.5 ml is approximately  $100 \text{ nmol } \sqrt{s}$ . Microfluidic NMR systems can make use of miniaturised NMR detectors, which benefit from a favourable scaling of the mass sensitivity with detection volume [8, 26, 101]. At a size scale of  $2.5 \mu\text{l}$ , a mass sensitivity around  $1 \text{ nmol } \sqrt{s}$  has been reported [10]. However, due to the limited volume in such systems, the *concentration* sensitivity is very poor, such that only compounds present at mM levels can be quantified in microfluidic NMR systems. This situation gets worse as the detector volume decreases. By contrast, many

samples of interest, such as metabolites in microfluidic culture systems, are only present at  $\mu\text{M}$  levels.

In the present case, the concentration limit of detection from Eqn. ?? is

$$\text{cLOD}_\omega = \frac{\text{nLOD}_\omega}{V_s} = (0.88 \pm 0.16)\mu\text{M}\sqrt{s}. \quad (1.26)$$

From the ratio of the signal intensities in the thermal and hyperpolarized spectra shown in Fig. 1.17a and b, it is possible to estimate the  $^1\text{H}$  polarization levels. In the thermal spectrum, the SNR is about 5:1, whereas it is 400:1 in the hyperpolarized spectrum. The thermal spectrum is obtained from 512 transients, therefore the single transient thermal SNR would be  $5/\sqrt{512} \approx 0.22$ . This leads to a signal enhancement factor of  $\epsilon \approx 400/0.22 \approx 1800$ .

This can be compared to the expected signal enhancement given the enrichment level of para-hydrogen used in the experiment. The ideal enhancement factor is given by

$$\epsilon_{id} = \frac{4x_p - 1}{3\sqrt{2}} \frac{2k_B T}{\hbar\gamma B_0}, \quad (1.27)$$

where  $x_p$  is the mole fraction of parahydrogen in the feed gas,  $\gamma$  is the magnetogyric ratio,  $B_0$  is the magnetic field, and  $\hbar$  and  $k_B$  are Planck's and Boltzmann's constants, respectively. The factor  $\frac{1}{\sqrt{2}}$  reflects the use of a  $\pi/4$  pulse for the hyperpolarized experiment. At a temperature of  $T = 298$  K and a magnetic field of 11.7 T, and with  $x_p = 0.5$ , this yields  $\epsilon_{id} \approx 5900$ , which is a factor of 3.3 larger than the experimentally observed enhancement factor. We can therefore conclude that about 2/3 of the theoretically available spin order is lost to relaxation under the present experimental conditions.

### 1.6.8 2D NMR

A great advantage of the continuously operating microfluidic PHIP system is the ability to acquire many transients in succession under virtually unchanged conditions. This is difficult to achieve with bubbling hydrogen through a solution. As a consequence, hyperpolarized multi-dimensional NMR spectra[60, 62–64, 102, 103]. have been recorded either using automated reactors combined with NMR flow probes,[63, 64] or using ultrafast acquisition techniques[62, 102, 103].

The PHIP@chip setup allows straightforward acquisition of 2D spectra, using conventional  $t_1$  incrementation. To demonstrate this, we have taken 2D TOCSY (Total Correlation Spectroscopy) and HMQC (Heteronuclear Multiple Quantum Coherence) NMR spectra of the reaction mixture at a flow rate of  $8 \text{ L min}^{-1}$ . The conventional pulse

sequences were modified by replacing the initial  $\pi/2$  pulse with a  $\pi/4$  pulse; we refer to these experiments as “PH-TOCSY” (parahydrogen TOCSY) and “PH-HMQC” (parahydrogen HMQC).

A PH-TOCSY spectrum acquired in 20 min is shown in Fig. 1.18a. A *thermal equilibrium* TOCSY spectrum of this compound would be expected to contain diagonal peaks connecting the identical nuclear spins in the two acquisition dimensions, and off-diagonal peaks connecting  $J$ -coupled spins. In the PH-TOCSY experiment, the diagonal peaks only appear for the two parahydrogen proton signals, because they are the only spins significantly polarised in the indirect dimension. The other protons are only polarised during the isotropic spin-mixing step of the pulse sequence, and hence do not appear in the indirect dimension. These protons only produce off-diagonal peaks, connecting them to the parahydrogen pair. As shown in Fig. 1.18b, the simulated spectrum closely corresponds to the experimentally observed one.

We would expect a *thermal equilibrium* TOSCY spectrum of this compound to contain diagonal peaks connecting the identical nuclear spins in the two acquisition dimensions, and off-diagonal peaks connecting  $J$ -coupled spins. In this *hyperpolarized* experiment, the diagonal peaks only appear for the two parahydrogen proton signals, because they are the only spins significantly polarised in the direct detection dimension. The other protons are only polarised during the isotropic spin-mixing step of the pulse sequence, and hence don’t appear in the direct dimension. These protons only produce off-diagonal peaks, connecting them to the parahydrogen pair.

A PH-HMQC spectrum acquired in 60 min is shown in Fig. 1.18c. It contains two peaks, linking the parahydrogen protons to the  $^{13}\text{C}$  spins to which they have a direct  $^1J_{\text{CH}}$  coupling. An experiment of this kind, in which signals are detected at full natural abundance of the  $^{13}\text{C}$  spins (about 1%) in a  $2.5 \mu\text{L}$  detection volume, is only possible due to both the high polarization levels and stability of the system.

The results in Fig. 1.18 show that the hyperpolarized spin order can be spread to other protons in the molecule by the application of the isotropic mixing sequence MLEV-17 [104, 105] prior to 1D signal acquisition. This simple trick allows one to hyperpolarise any protons that are  $J$ -coupled to the parahydrogen pair, which makes the technique more general.

Much ongoing research in the field of hyperpolarization is motivated by in-vivo applications, where hyperpolarized compounds are used as magnetic resonance imaging contrast agents [106]. Mostly, this involves transferring the nuclear spin polarization after hydrogenation to other nuclei ( $^{13}\text{C}$ ,  $^{15}\text{N}$ ,  $^{31}\text{P}$ ) with lower magnetogyric ratios, where spin-lattice relaxation times are longer. [57, 107, 108] Many of these approaches use zero or very low magnetic fields for hydrogenation and polarization transfer. This has the advantage that near magnetic equivalence between the two added protons is maintained through the reaction, leading to longer lifetimes [53–58, 109, 110]. The present

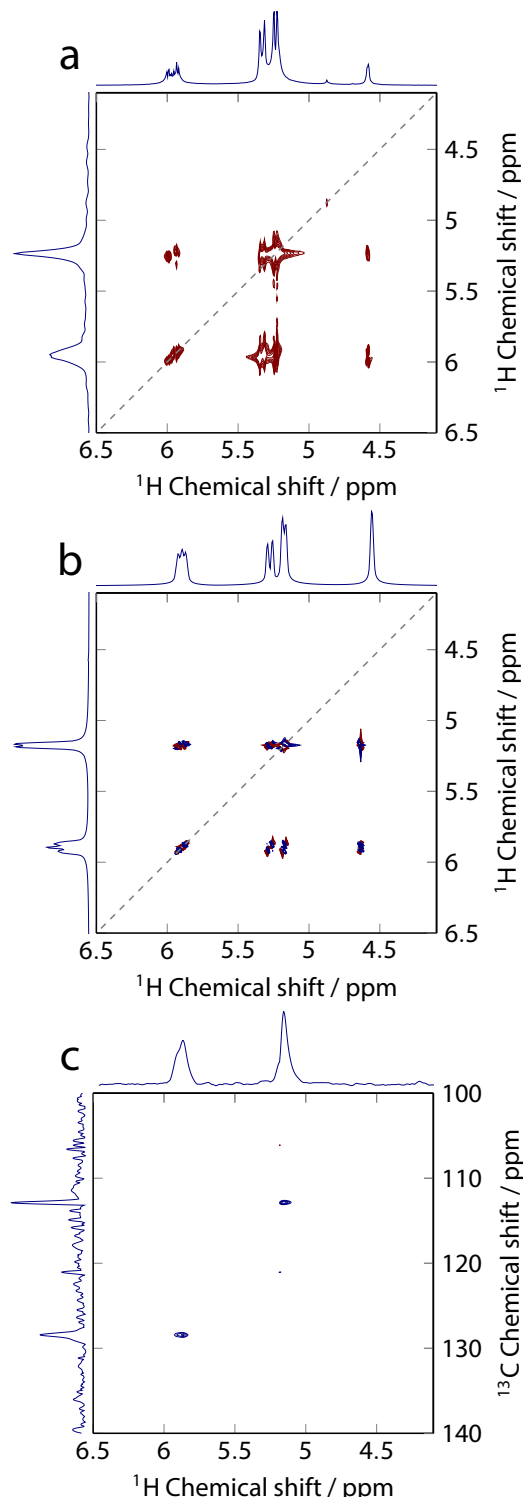


FIGURE 1.18: The continuous flow PHIP@chip approach allows acquisition of two-dimensional spectra with very high sensitivity. a: PH-TOCSY spectrum of the hyperpolarized reaction mixture, flowing at  $8 \mu\text{L min}^{-1}$ . b: Simulated PH-TOCSY spectrum. The diagonal in the spectrum is marked by a dashed grey line. Only the protons originating from parahydrogen give signals on the diagonal; the polarization is transferred to the other locations by the isotropic mixing sequence. Both PH-TOCSY spectra are plotted in magnitude mode. c:  $^1\text{H}-^{13}\text{C}$  PH-HMOC spectrum showing two separate multiplets, each correlating one of the two hyperpolarized protons with the directly bonded  $^{13}\text{C}$  spin.

work opens a complementary strategy, in that the hydrogenation is done at high field. Deleterious effects of relaxation are minimised by the proximity of the site of hydrogenation to the point of use. Arguably, this approach has advantages in the context of microfluidic systems, where only small quantities of hyperpolarized agents are needed.

## 1.7 Conclusions

The combination of a highly efficient transmission-line NMR micro detector with parahydrogen-induced hyperpolarization leads to an unprecedented sensitivity in inductively detected NMR, with a mass limit of detection around  $2.2 \text{ pmol} \sqrt{\text{s}}$ . This corresponds to a concentration sensitivity of less than  $1 \mu\text{M} \sqrt{\text{s}}$ , which, to our knowledge, has not previously been reached at the volume scale of  $2.5 \mu\text{L}$ . This opens the perspective to be able to study chemical processes involving low-abundance species in mass-limited samples. Obviously, such applications require preparation of a hyperpolarized reactant. As the foregoing study shows, the necessary chemistry can be integrated in a microfluidic system. It should be noted that parahydrogen enriched to 50% (compared to 25% at thermal equilibrium) has been used; the sensitivity could easily be boosted by a factor of three by using pure parahydrogen. Microfluidic systems hold great potential in combination with hyperpolarized NMR. All hyperpolarization techniques require coordinated manipulation of fluids and spin transformations. The results shown in the foregoing demonstrate that in the case of parahydrogen-induced polarization, this can be assisted considerably by integrating some of the necessary chemical steps on a microfluidic chip. Parahydrogen can be delivered to a reactive solution through a PDMS membrane at sufficient rate to achieve significant levels of hyperpolarization; dissolution and transport of hydrogen in PDMS does not appear to lead to significant ortho-para equilibration. The highly stable continuous operation of the PHIP@chip system allows quantitative studies of the hydrogenation kinetics, and the relevant relaxation processes. This is demonstrated by the dependence of the steady-state signal intensity on flow rate and the recovery of the hyperpolarized signal after saturation (Fig. 1.15).

The successful demonstration of PHIP on a chip opens important perspectives. Conditions can be optimised for continued production of hyperpolarized metabolites, which opens the possibility to conduct in-situ metabolic studies in microfluidic cultures of cells, tissues, and organisms. While the hyperpolarized compound used here, allyl acetate, is not a metabolite per se, the production of hyperpolarized metabolic species through PHIP has been demonstrated before [49, 56, 58, 111–113]. Some metabolites, such as fumarate, can be generated directly by hydrogenation of an unsaturated precursor [112]. Aime et al. have proposed a more generally applicable method [111], which relies on the metabolite bound to an alkyne sidearm through an ester linkage. After hydrogenation, the polarization is transferred to a  $^{13}\text{C}$  nucleus in the metabolic moiety, and the sidearm is cleaved. PHIP@chip opens the possibility of implementing these additional production

steps on the same chip. While previous demonstrations of sidearm hydrogenation have been carried out at low magnetic field, it may be possible to adapt recently developed efficient methods for heteronuclear polarization transfer at high field[59] to this purpose. In turn, this may enable integration of the hyperpolarized metabolite generation with an on-chip culture of cells or other biological systems. Thanks to its stability, the setup provides a convenient means to optimise pulse sequences and reaction conditions for producing hyperpolarized targets.

The successful demonstration of PHIP on a chip opens important perspectives. Conditions can be optimised for continued production of hyperpolarized metabolites, which opens the possibility to conduct in-situ metabolic studies in microfluidic cultures of cells, tissues, and organisms. While the hyperpolarized compound used here, allyl acetate, is not a metabolite per se, the production of hyperpolarized metabolic species through PHIP has been demonstrated before [56, 58, 106, 111–113]. Some metabolites, such as Fumarate [112], can be generated directly by hydrogenation of an unsaturated precursor. Aime et al. have proposed a more generally applicable method [111], which relies on the metabolite bound to an alkyne sidearm through an ester linkage. After hydrogenation, the polarization is transferred to a  $^{13}\text{C}$  nucleus in the metabolic moiety, and the sidearm is cleaved. PHIP@chip opens the possiblity of implementing these additional production steps on the same chip. In turn, this may enable integration of the hyperpolarized metabolite generation with an on-chip culture of cells or other biological systems. Thanks to its stability, the setup provides a convenient means to optimise pulse sequences and reaction conditions for producing hyperpolarized targets.



# Bibliography

- [1] J. Eills, W. Hale, M. Sharma, M. Rossetto, M. H. Levitt and M. Utz, *Journal of the American Chemical Society*, 0, **0**, null.
- [2] M. Maiwald, H. H. Fischer, Y.-K. Kim, K. Albert and H. Hasse, *J. Magn. Reson.*, 2004, **166**, 135–146.
- [3] D. A. Foley, E. Bez, A. Codina, K. L. Colson, M. Fey, R. Krull, D. Piroli, M. T. Zell and B. L. Marquez, *Analytical chemistry*, 2014, **86**, 12008–12013.
- [4] D. S. Wishart, *TrAC Trends in Analytical Chemistry*, 2008, **27**, 228–237.
- [5] M. Gottschalk, G. Ivanova, D. M. Collins, A. Eustace, R. O'Connor and D. F. Brougham, *NMR in Biomedicine*, 2008, **21**, 809–819.
- [6] M. Cuperlovic-Culf, D. A. Barnett, A. S. Culf and I. Chute, *Drug Discovery Today*, 2010, **15**, 610–621.
- [7] L. Shintu, R. Baudoin, V. Navratil, J. M. Prot, C. Pontoizeau, M. Defernez, B. J. Blaise, C. Domange, A. R. R. Péry and P. Toulhoat, *Analytical chemistry*, 2012.
- [8] D. Olson, T. Peck, A. Webb, R. Magin and J. Sweedler, *Science*, 1995, **270**, 1967–1970.
- [9] J. Bart, A. J. Kolkman, A. J. Oosthoek-de Vries, K. Koch, P. J. Nieuwland, H. J. W. G. Janssen, P. J. M. van Bentum, K. A. M. Ampt, F. P. J. T. Rutjes, S. S. Wijmenga, H. J. G. E. Gardeniers and A. P. M. Kentgens, *J Am Chem Soc*, 2009, **131**, 5014–5015.
- [10] G. Finch, A. Yilmaz and M. Utz, *Journal of Magnetic Resonance*, 2016, **262**, 73–80.
- [11] J. Wang, G. Sui, V. P. Mocharla, R. J. Lin, M. E. Phelps, H. C. Kolb and H.-R. Tseng, *Angew. Chem.*, 2006, **118**, 5402–5407.
- [12] A. B. Theberge, E. Mayot, A. El Harrak, F. Kleinschmidt, W. T. S. Huck and A. D. Griffiths, *Lab Chip*, 2012, **12**, 1320–1326.

- [13] P. H. Hoang, C. T. Nguyen, J. Perumal and D.-P. Kim, *Lab Chip*, 2011, **11**, 329–335.
- [14] K. i. Ohno, K. Tachikawa and A. Manz, *Electrophoresis*, 2008, **29**, 4443–4453.
- [15] X. Zhou, S. Cai, A. Hong, Q. You, P. Yu, N. Sheng, O. Srivannavit, S. Muranjan, J. M. Rouillard and Y. Xia, *Nucleic acids research*, 2004, **32**, 5409–5417.
- [16] H. Fang, Y. Sun, X. Wang, M. Sharma, Z. Chen, X. Cao, M. Utz and Z. Tian, *Sci. China Chem.*, 2018, **61**, 1460–1464.
- [17] P. H. Hoang, H. Park and D.-P. Kim, *J Am Chem Soc*, 2011, **133**, 14765–14770.
- [18] A. Günther and K. Jensen, *Lab Chip*, 2006, **6**, 1487–1503.
- [19] A. Manz, N. Graber and H. WIDMER, *Sensor Actuat B-Chem*, 1990, **1**, 244–248.
- [20] G. M. Whitesides, *Nature*, 2006, **442**, 368–373.
- [21] J. El-Ali, P. K. Sorger and K. F. Jensen, *Nature*, 2006, **442**, 403–411.
- [22] J. West, M. Becker, S. Tombrink and A. Manz, *Analytical chemistry*, 2008, **80**, 4403–4419.
- [23] P. Neužil, S. Giselbrecht, K. Länge, T. J. Huang and A. Manz, *Nature Reviews Drug Discovery*, 2012, **11**, 620–632.
- [24] A. D. Gracz, I. A. Williamson, K. C. Roche, M. J. Johnston, F. Wang, Y. Wang, P. J. Attayek, J. Balowski, X. F. Liu, R. J. Laurenza, L. T. Gaynor, C. E. Sims, J. A. Galanko, L. Li, N. L. Allbritton and S. T. Magness, *Nature Cell Biology*, 2015, **17**, 340–349.
- [25] H. Ryan, S.-H. Song, A. Zaß, J. Korvink and M. Utz, *Anal. Chem.*, 2012, **84**, 3696–3702.
- [26] V. Badilita, R. C. Meier, N. Spengler, U. Wallrabe, M. Utz and J. G. Korvink, *Soft Matter*, 2012, **8**, 10583–10597.
- [27] N. Spengler, A. Moazenzadeh, R. C. Meier, V. Badilita, J. G. Korvink and U. Wallrabe, *J. Micromech. Microeng.*, 2014, **24**, 034004.
- [28] D. Rugar, C. S. Yannoni and J. Sidles, *Nature*, 1992, **360**, 563–566.
- [29] D. Rugar, R. Budakian, H. J. Mamin and B. W. Chui, *Nature*, 2004, **430**, 329–332.
- [30] H. J. Mamin, M. Poggio, C. L. Degen and D. Rugar, *Nature Nanotech*, 2007, **2**, 301–306.
- [31] M. Poggio and C. L. Degen, *Nanotechnology*, 2010, **21**, 342001.

- [32] J. R. Maze, P. L. Stanwix, J. S. Hodges, S. Hong, J. M. Taylor, P. Cappellaro, L. Jiang, M. V. G. Dutt, E. Togan, A. S. Zibrov, A. Yacoby, R. L. Walsworth and M. D. Lukin, *Nature*, 2008, **455**, 644–647.
- [33] T. Staudacher, F. Shi, S. Pezzagna, J. Meijer, J. Du, C. A. Meriles, F. Reinhard and J. Wrachtrup, *Science*, 2013, **339**, 561–563.
- [34] D. Rugar, H. J. Mamin, M. H. Sherwood, M. Kim, C. T. Rettner, K. Ohno and D. D. Awschalom, *Nature Nanotech*, 2015, **10**, 120–124.
- [35] R. McDermott, A. H. Trabesinger, M. Mück, E. L. Hahn, A. Pines and J. Clarke, *Science*, 2002, **295**, 2247–2249.
- [36] D. Budker and M. Romalis, *NATURE PHYSICS*, 2007, **3**, 227–234.
- [37] S. Xu, V. V. Yashchuk, M. H. Donaldson, S. M. Rochester, D. Budker and A. Pines, *Proceedings of the National Academy of Sciences*, 2006, **103**, 12668–12671.
- [38] J. W. Blanchard, M. P. Ledbetter, T. Theis, M. C. Butler, D. Budker and A. Pines, *J Am Chem Soc*, 2013, **135**, 3607–3612.
- [39] D. R. Glenn, D. B. Bucher, J. Lee, M. D. Lukin, H. Park and R. L. Walsworth, *Nature*, 2018, **555**, 351–354.
- [40] K. Münnemann and H. W. Spiess, *Nature Physics*, 2011, **7**, 522.
- [41] E. McDonnell, S. Han, C. Hilty, K. Pierce and A. Pines, *Anal. Chem.*, 2005, **77**, 8109–8114.
- [42] H. Desvaux, D. J. Y. Marion, G. Huber and P. Berthault, *Angewandte Chemie International Edition*, 2009, **48**, 4341–4343.
- [43] V.-V. Telkki, V. V. Zhivonitko, S. Ahola, K. V. Kovtunov, J. Jokisaari and I. V. Koptyug, *Angewandte Chemie International Edition*, 2010, **49**, 8363–8366.
- [44] E. Paciok and B. Blümich, *ANGEWANDTE CHEMIE-INTERNATIONAL EDITION IN ENGLISH-*, 2011, **50**, 5258–5260.
- [45] R. Jiménez-Martínez, D. J. Kennedy, M. Rosenbluh, E. A. Donley, S. Knappe, S. J. Seltzer, H. L. Ring, V. S. Bajaj and J. Kitching, *Nature Communications*, 2014, **5**, 3908.
- [46] A. Causier, G. Carret, C. Boutin, T. Berthelot and P. Berthault, *Lab Chip*, 2015, **15**, 2049–2054.
- [47] W. Hale, J. Eills, M. Rossetto, M. Levitt and M. Utz, Oral presentation, Euromar conference, Nantes, 2018.

- [48] L. Bordonali, N. Nordin, E. Fuhrer, N. MacKinnon and J. G. Korvink, *Lab Chip*, 2019, **19**, 503–512.
- [49] J.-B. Hövener, A. N. Pravdivtsev, B. Kidd, C. R. Bowers, S. Glöggler, K. V. Kovtunov, M. Plaumann, R. Katz-Brull, K. Buckenmaier and A. Jerschow, *Angewandte Chemie International Edition*, 2018, **57**, 11140–11162.
- [50] S. B. Duckett and R. E. Mewis, *Accounts of chemical research*, 2012, **45**, 1247–1257.
- [51] S. Glöggler, J. Colell and S. Appelt, *Journal of Magnetic Resonance*, 2013, **235**, 130–142.
- [52] R. A. Green, R. W. Adams, S. B. Duckett, R. E. Mewis, D. C. Williamson and G. G. Green, *Progress in nuclear magnetic resonance spectroscopy*, 2012, 1–48.
- [53] P. Bhattacharya, E. Y. Chekmenev, W. H. Perman, K. C. Harris, A. P. Lin, V. A. Norton, C. T. Tan, B. D. Ross and D. P. Weitekamp, *Journal of magnetic resonance*, 2007, **186**, 150–155.
- [54] E. Y. Chekmenev, J. Hövener, V. A. Norton, K. Harris, L. S. Batchelder, P. Bhattacharya, B. D. Ross and D. P. Weitekamp, *Journal of the American Chemical Society*, 2008, **130**, 4212–4213.
- [55] E. Y. Chekmenev, V. A. Norton, D. P. Weitekamp and P. Bhattacharya, *Journal of the American Chemical Society*, 2009, **131**, 3164–3165.
- [56] R. V. Shchepin, A. M. Coffey, K. W. Waddell and E. Y. Chekmenev, *Analytical chemistry*, 2014, **86**, 5601–5605.
- [57] F. Reineri, T. Boi and S. Aime, *Nature Communications*, 2015, **6**, 5858.
- [58] E. Cavallari, C. Carrera, M. Sorge, G. Bonne, A. Muchir, S. Aime and F. Reineri, *Scientific reports*, 2018, **8**, 8366.
- [59] J. Eills, G. Stevanato, C. Bengs, S. Glöggler, S. J. Elliott, J. Alonso-Valdesueiro, G. Pileio and M. H. Levitt, *Journal of Magnetic Resonance*, 2017, **274**, 163–172.
- [60] M. Roth, P. Kindervater, H. P. Raich, J. Bargon, H. W. Spiess and K. Münnemann, *Angew. Chem.*, 2010, **122**, 8536–8540.
- [61] S. Lehmkuhl, M. Wiese, L. Schubert, M. Held, M. Küppers, M. Wessling and B. Blümich, *Journal of Magnetic Resonance*, 2018, **291**, 8–13.
- [62] P. Giraudeau, Y. Shrot and L. Frydman, *J Am Chem Soc*, 2009, **131**, 13902–13903.
- [63] L. S. Lloyd, R. W. Adams, M. Bernstein, S. Coombes, S. B. Duckett, G. G. R. Green, R. J. Lewis, R. E. Mewis and C. J. Sleigh, *J Am Chem Soc*, 2012, **134**, 12904–12907.

- [64] N. Eshuis, R. L. E. G. Aspers, B. J. A. van Weerdenburg, M. C. Feiters, F. P. J. T. Rutjes, S. S. Wijmenga and M. Tessari, *Angew. Chem.*, 2015, **127**, 14735–14738.
- [65] M. E. Halse, *TrAC Trends in Analytical Chemistry*, 2016, **83**, 76–83.
- [66] L. Schröder, T. J. Lowery, C. Hilty, D. E. Wemmer and A. Pines, *Science*, 2006, **314**, 446–449.
- [67] K. Golman and M. Thaning, *Proceedings of the National Academy of Sciences*, 2006, **103**, 11270–11275.
- [68] K. Ruppert, K. Qing, J. T. Patrie, T. A. Altes and J. P. Mugler III, *Academic radiology*, 2019, **26**, 355–366.
- [69] W. Zha, S. K. Nagle, R. V. Cadman, M. L. Schiebler and S. B. Fain, *Radiology*, 2018, **290**, 229–237.
- [70] Q. Chappuis, J. Milani, B. Vuichoud, A. Bornet, A. D. Gossert, G. Bodenhausen and S. Jannin, *The journal of physical chemistry letters*, 2015, **6**, 1674–1678.
- [71] Y. Kim, M. Liu and C. Hilty, *Analytical chemistry*, 2016, **88**, 11178–11183.
- [72] H. Allouche-Arnon, A. Gamliel, C. M. Barzilay, R. Nalbandian, J. M. Gomori, M. Karlsson, M. H. Lerche and R. Katz-Bruylants, *Contrast media molecular imaging*, 2011, **6**, 139–147.
- [73] Y. Lee, G. S. Heo, H. Zeng, K. L. Wooley and C. Hilty, *Journal of the American Chemical Society*, 2013, **135**, 4636–4639.
- [74] M. Duewel, N. Vogel, C. K. Weiss, K. Landfester, H.-W. Spiess and K. Münnemann, *Macromolecules*, 2012, **45**, 1839–1846.
- [75] A. Bornet, M. Maucourt, C. Deborde, D. Jacob, J. Milani, B. Vuichoud, X. Ji, J.-N. Dumez, A. Moing and G. Bodenhausen, *Analytical chemistry*, 2016, **88**, 6179–6183.
- [76] N. Zacharias, J. Lee, S. Ramachandran, S. Shanmugavelandy, J. McHenry, P. Dutta, S. Millward, S. Gammon, E. Efstatthiou and P. Troncoso, *Molecular Imaging and Biology*, 2019, **21**, 86–94.
- [77] I. Romanenko, D. Gajan, R. Sayah, D. Crozet, E. Jeanneau, C. Lucas, L. Leroux, L. Veyre, A. Lesage and L. Emsley, *Angewandte Chemie International Edition*, 2015, **54**, 12937–12941.
- [78] T. Ong, W. Liao, V. Mougel, D. Gajan, A. Lesage, L. Emsley and C. Copéret, *Angewandte Chemie International Edition*, 2016, **55**, 4743–4747.
- [79] Y. Geiger, H. E. Gottlieb, U. Akbey, H. Oschkinat and G. Goobes, *Journal of the American Chemical Society*, 2016, **138**, 5561–5567.

- [80] L. Piveteau, T.-C. Ong, A. J. Rossini, L. Emsley, C. Coperet and M. V. Kovalenko, *Journal of the American Chemical Society*, 2015, **137**, 13964–13971.
- [81] Z. J. Berkson, R. J. Messinger, K. Na, Y. Seo, R. Ryoo and B. F. Chmelka, *Angewandte Chemie*, 2017, **129**, 5246–5251.
- [82] M. L. Hirsch, N. Kalechofsky, A. Belzer, M. Rosay and J. G. Kempf, *Journal of the American Chemical Society*, 2015, **137**, 8428–8434.
- [83] D. T. Peat, M. L. Hirsch, D. G. Gadian, A. J. Horsewill, J. R. Owers-Bradley and J. G. Kempf, *Physical Chemistry Chemical Physics*, 2016, **18**, 19173–19182.
- [84] G. Liu, M. Levien, N. Karschin, G. Parigi, C. Luchinat and M. Bennati, *Nature chemistry*, 2017, **9**, 676.
- [85] K. J. Pike, T. F. Kemp, H. Takahashi, R. Day, A. P. Howes, E. V. Kryukov, J. F. MacDonald, A. E. Collis, D. R. Bolton and R. J. Wylde, *Journal of Magnetic Resonance*, 2012, **215**, 1–9.
- [86] M. Sharma, G. Janssen, J. Leggett, A. Kentgens and P. van Bentum, *Journal of Magnetic Resonance*, 2015, **258**, 40–48.
- [87] J. H. Ardenkjær-Larsen, B. Fridlund, A. Gram, G. Hansson, L. Hansson, M. H. Lerche, R. Servin, M. Thaning and K. Golman, *Proceedings of the National Academy of Sciences*, 2003, **100**, 10158–10163.
- [88] D. A. Barskiy, A. M. Coffey, P. Nikolaou, D. M. Mikhaylov, B. M. Goodson, R. T. Branca, G. J. Lu, M. G. Shapiro, V.-V. Telkki, V. V. Zhivonitko *et al.*, *Chemistry—A European Journal*, 2017, **23**, 725–751.
- [89] R. A. Green, R. W. Adams, S. B. Duckett, R. E. Mewis, D. C. Williamson and G. G. Green, *Progress in Nuclear Magnetic Resonance Spectroscopy*, 2012, **67**, 1 – 48.
- [90] A. Gamliel, H. Allouche-Arnon, R. Nalbandian, C. M. Barzilay, J. M. Gomori and R. Katz-Bruell, *Applied Magnetic Resonance*, 2010, **39**, 329–345.
- [91] B. Feng, A. M. Coffey, R. D. Colon, E. Y. Chekmenev and K. W. Waddell, *Journal of Magnetic Resonance*, 2012, **214**, 258–262.
- [92] C. R. Bowers and D. P. Weitekamp, *Journal of the American Chemical Society*, 1987, **109**, 5541–5542.
- [93] M. G. Pravica and D. P. Weitekamp, *Chemical Physics Letters*, 1988, **145**, 255–258.
- [94] R. Zhou, W. Cheng, L. M. Neal, E. W. Zhao, K. Ludden, H. E. Hagelin-Weaver and C. R. Bowers, *Physical Chemistry Chemical Physics*, 2015, **17**, 26121–26129.

- [95] A. Yilmaz and M. Utz, *Lab Chip*, 2016, **16**, 2079–2085.
- [96] M. Sharma and M. Utz, *Journal of Magnetic Resonance*, 2019.
- [97] J. Bezanson, A. Edelman, S. Karpinski and V. B. Shah, *SIAM Rev.*, 2017, **59**, 65–98.
- [98] E. Cavallari, C. Carrera, T. Boi, S. Aime and F. Reineri, *The Journal of Physical Chemistry B*, 2015, **119**, 10035–10041.
- [99] L. Bordonali, N. Nordin, E. Fuhrer, N. MacKinnon and J. G. Korvink, *Lab Chip*, 2019, **19**, 503–512.
- [100] M. Mompeán, R. M. Sánchez-Donoso, A. Hoz, V. Saggiomo, A. H. Velders and M. V. Gomez, *Nature communications*, 2018, **9**, 108.
- [101] S. S. Zalesskiy, E. Danieli, B. Blümich and V. P. Ananikov, *Chem. Rev.*, 2014, **114**, 5641–5694.
- [102] M. Mishkovsky and L. Frydman, *Chemphyschem*, 2008, **9**, 2340–2348.
- [103] A. S. Kiryutin, G. Sauer, D. Tietze, M. Brodrecht, S. Knecht, A. V. Yurkovskaya, K. L. Ivanov, O. Avrutina, H. Kolmar and G. Buntkowsky, *Chemistry - A European Journal*, 2019, **32**, 211–7.
- [104] M. H. Levitt, R. Freeman and T. Frenkel, *Journal of Magnetic Resonance (1969)*, 1982, **50**, 157–160.
- [105] A. Bax and D. G. Davis, *Journal of Magnetic Resonance (1969)*, 1985, **65**, 355–360.
- [106] J. Hovener, A. N. Pravdivtsev, B. Kidd, C. R. Bowers, S. Glöggler, K. V. Kovtunov, M. Plaumann, R. Katz-Brull, K. Buckenmaier, A. Jerschow, F. Reineri, T. Theis, R. V. Shchepin, S. Wagner, N. M. M. Zacharias, P. Bhattacharya and E. Y. Chekmenev, *Angew. Chem.*, 2018.
- [107] M. Goldman, H. Johannesson, O. Axelsson and M. Karlsson, *Magn Reson Imaging*, 2005, **23**, 153–157.
- [108] M. Goldman, H. Johannesson, O. Axelsson and M. Karlsson, *Comptes Rendus Chimie*, 2006, **9**, 357–363.
- [109] B. Ripka, J. Eills, H. Kouřilová, M. Leutzsch, M. H. Levitt and K. Münnemann, *Chemical Communications*, 2018.
- [110] S. S. Roy, K. M. Appleby, E. J. Fear and S. B. Duckett, *The journal of physical chemistry letters*, 2018, **9**, 1112–1117.
- [111] F. Reineri, T. Boi and S. Aime, *Nature communications*, 2015, **6**, 5858.

- 
- [112] B. Ripka, J. Eills, H. Kouřilová, M. Leutzsch, M. H. Levitt and K. Münnemann, *Chem. Commun.*, 2018, **54**, 12246–12249.
  - [113] S. Korchak, S. Yang, S. Mamone and S. Glöggler, *ChemistryOpen*, 2018, **7**, 344–348.